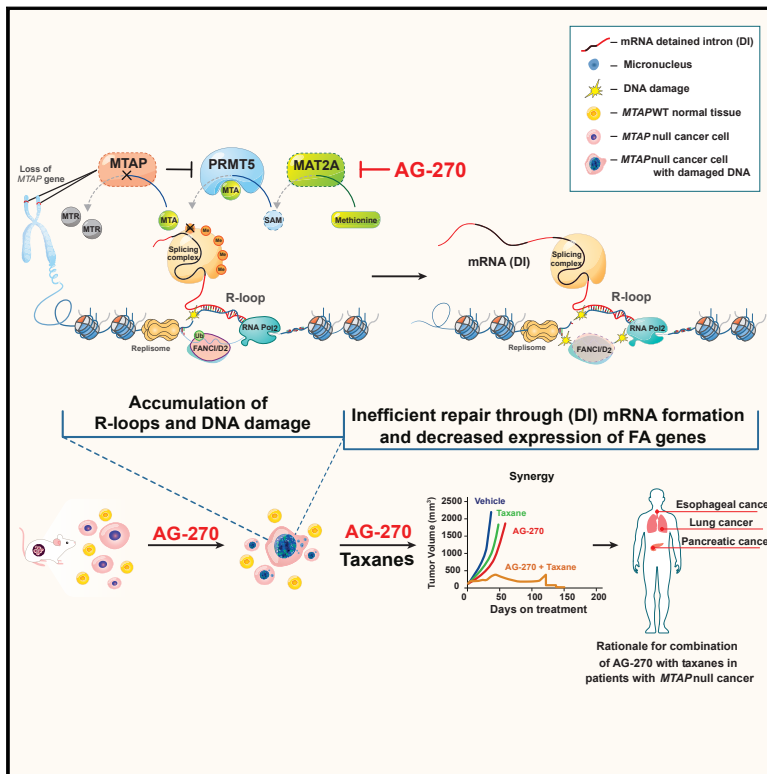


Cancer Cell

MAT2A Inhibition Blocks the Growth of *MTAP*-Deleted Cancer Cells by Reducing PRMT5-Dependent mRNA Splicing and Inducing DNA Damage

Graphical Abstract



Highlights

- Development of MAT2A inhibitors (MAT2Ai) AGI-24512 and AG-270 with improved potency
- AGI-24512 and AG-270 reduce proliferation of cancer cells and tumors that lack MTAP
- MAT2Ai reduce PRMT5 activity affecting mRNA splicing and inducing DNA damage
- Antiproliferative effects of AG-270 are synergistic with taxanes *in vitro* and *in vivo*

Authors

Peter Kalev, Marc L. Hyer, Stefan Gross, ..., Jeremy Travins, Kevin M. Marks, Katya Marjon

Correspondence

katya.marjon@agios.com

In Brief

Kalev et al. characterize potent inhibitors of the metabolic enzyme MAT2A, including the clinical candidate AG-270, which reduces proliferation of *MTAP*-deficient cancer cells and tumors. This is mediated by deregulation of splicing, DNA damage, and reduced DNA damage repair, enabling synergistic combinations with antimetabolic taxanes.



Article

MAT2A Inhibition Blocks the Growth of *MTAP*-Deleted Cancer Cells by Reducing PRMT5-Dependent mRNA Splicing and Inducing DNA Damage

Peter Kaley,^{1,16} Marc L. Hyer,^{2,16} Stefan Gross,³ Zenon Konteatis,⁴ Chi-Chao Chen,⁵ Mark Fletcher,⁵ Max Lein,⁶ Elia Aguado-Fraile,⁷ Victoria Frank,¹ Amelia Barnett,¹ Everton Mandley,² Joshua Goldford,⁸ Yue Chen,⁶ Katie Sellers,^{8,11} Sebastian Hayes,⁸ Kate Lizotte,⁸ Phong Quang,^{1,12} Yesim Tuncay,¹ Michelle Clasquin,^{8,13} Rachel Peters,⁹ Jaclyn Weier,¹ Eric Simone,¹⁰ Joshua Murtie,^{1,2} Wei Liu,⁵ Raj Nagaraja,⁶ Lenny Dang,³ Zhihua Sui,⁴ Scott A. Biller,⁴ Jeremy Travins,^{4,14} Kevin M. Marks,^{1,15} and Katya Marjon^{1,17,*}

¹Biology, Agios Pharmaceuticals, Inc., Cambridge, MA 02139, USA

²Pharmacology, Agios Pharmaceuticals, Inc., Cambridge, MA 02139, USA

³Biochemistry and Biophysics, Agios Pharmaceuticals, Inc., Cambridge, MA 02139, USA

⁴Chemistry, Agios Pharmaceuticals, Inc., Cambridge, MA 02139, USA

⁵Bioinformatics, Agios Pharmaceuticals, Inc., Cambridge, MA 02139, USA

⁶Drug Metabolism and Pharmacokinetics, Agios Pharmaceuticals, Inc., Cambridge, MA 02139, USA

⁷Clinical Biomarkers, Agios Pharmaceuticals, Inc., Cambridge, MA 02139, USA

⁸Cell Metabolism, Agios Pharmaceuticals, Inc., Cambridge, MA 02139, USA

⁹Toxicology, Agios Pharmaceuticals, Inc., Cambridge, MA 02139, USA

¹⁰Chemistry, Manufacturing and Control, Agios Pharmaceuticals, Inc., Cambridge, MA 02139, USA

¹¹Present address: Rheos Medicines, Cambridge, MA 02142, USA

¹²Present address: Exploratory Biology, Novartis Institutes for Biomedical Research, Cambridge, MA 02319, USA

¹³Present address: Internal Medicine Research Unit, Pfizer Inc., Cambridge, MA 02319, USA

¹⁴Present address: Chemistry, Takeda Pharmaceutical Co., Ltd., Lexington, MA 02421, USA

¹⁵Present address: Novartis Institutes for Biomedical Research, Cambridge, MA 02139, USA

¹⁶These authors contributed equally

¹⁷Lead Contact

*Correspondence: katya.marjon@agios.com

<https://doi.org/10.1016/j.ccell.2020.12.010>

SUMMARY

The methylthioadenosine phosphorylase (*MTAP*) gene is located adjacent to the cyclin-dependent kinase inhibitor 2A (*CDKN2A*) tumor-suppressor gene and is co-deleted with *CDKN2A* in approximately 15% of all cancers. This co-deletion leads to aggressive tumors with poor prognosis that lack effective, molecularly targeted therapies. The metabolic enzyme methionine adenosyltransferase 2 α (*MAT2A*) was identified as a synthetic lethal target in *MTAP*-deleted cancers. We report the characterization of potent *MAT2A* inhibitors that substantially reduce levels of *S*-adenosylmethionine (*SAM*) and demonstrate antiproliferative activity in *MTAP*-deleted cancer cells and tumors. Using RNA sequencing and proteomics, we demonstrate that *MAT2A* inhibition is mechanistically linked to reduced protein arginine methyltransferase 5 (*PRMT5*) activity and splicing perturbations. We further show that DNA damage and mitotic defects ensue upon *MAT2A* inhibition in HCT116 *MTAP*^{-/-} cells, providing a rationale for combining the *MAT2A* clinical candidate AG-270 with antimitotic taxanes.

INTRODUCTION

The metabolic enzyme methionine adenosyltransferase 2 α (*MAT2A*) has an important role in metabolism and epigenetics as the primary producer of the universal methyl donor *S*-adenosylmethionine (*SAM*). Despite this broad cellular role, recent work has shown that depletion of *MAT2A* leads to a selective antiproliferative effect in cancers with deletion of a separate metabolic gene, methylthioadenosine phosphorylase (*MTAP*)

(Kryukov et al., 2016; Marjon et al., 2016; Mavrakis et al., 2016). An explanation for this selective vulnerability could be that the activity of the *SAM*-utilizing type II arginine methyltransferase *PRMT5* is inhibited by a metabolite, 5'-methylthioadenosine (*MTA*), which accumulates when *MTAP* is deleted. Within the high-*MTA* environment of *MTAP*-deleted cancers, the catalytic activity of *PRMT5* is reduced and is sensitive to further inhibition by reduction in *SAM* levels (Marjon et al., 2016). While these results suggest that targeting *MAT2A* may prove beneficial



in *MTAP*-deleted cancers, past efforts to devise effective MAT2A inhibitors have been hampered by the presence of a large hydrophilic active site; a large, open, highly hydrophobic allosteric binding pocket; and by cellular adaptations that reduce the cellular potency of MAT2A inhibitors (Quinlan et al., 2017).

Methionine analogs such as cycloleucine (Lombardini et al., 1970; Lombardini and Sufrin, 1983) inhibit MAT2A *in vitro*, although their low potency and structural simplicity raise concerns about inhibitor specificity, and poor pharmacokinetics limit their use *in vivo*. A moderately potent allosteric MAT2A inhibitor, PF-9366, was recently discovered (Quinlan et al., 2017). However, PF-9366 treatment in cells induces cellular adaptation, including upregulation of MAT2A, which blunts its antiproliferative effects.

We developed *de novo* chemotype small-molecule inhibitors of MAT2A that are potent, cell permeable, and amenable to *in vivo* testing. Our optimized MAT2A inhibitors potently reduce SAM levels in cells by blocking *de novo* SAM biosynthesis. Using pharmacologic inhibitors of MAT2A, we validate MAT2A as a synthetic lethal target in *MTAP*-deleted cancers, demonstrating inhibition of cancer cell proliferation *in vitro* and tumor growth *in vivo*. Finally, we describe the biological consequences of MAT2A inhibition in *MTAP*-deleted cancer cells, including the genotype-selective impact on cellular PRMT5 activity and mRNA splicing, ultimately leading to cell-cycle defects and attenuated proliferation. Thus, targeting of MAT2A in *MTAP*-deleted cancers represents a successful application of synthetic lethality and a potential therapeutic approach for the substantial subset of patients with loss of the cyclin-dependent kinase inhibitor 2A (*CDKN2A*)/*MTAP* locus.

RESULTS

Cell-Based Activity of MAT2A Inhibitors

Small-molecule MAT2A inhibitors were identified by screening a library of >2,000 low-molecular-weight fragments for their ability to bind to MAT2A using a mass spectrometry-based ultrafiltration assay. Fragment hits with confirmed MAT2A binding in orthogonal enzymatic and surface plasmon resonance assays were co-crystallized with the MAT2A protein in complex with SAM. Further structure-guided design resulted in discovery of AGI-24512, a MAT2A inhibitor with an improvement in cell potency of 3–6 orders of magnitude compared with previously reported MAT2A inhibitors PF-9366 and cycloleucine (Figures 1A, 1B, and S1A).

To assess the specificity of its impact in cancer cells, we monitored the MAT2A product SAM after treatment with either AGI-24512 or a structurally related inactive compound (Figures 1A and 1C). Treatment with AGI-24512, but not the inactive control, led to a dose-dependent decrease in SAM levels, suggesting that the reduction in SAM was an on-target effect. Next, the rate of intracellular conversion of stable isotope-labeled $^{13}\text{C}_5$, ^{15}N -methionine to $^{13}\text{C}_5$, ^{15}N -SAM was assessed to directly measure the rate of SAM production in cells following short-term inhibitor treatment. AGI-24512 treatment led to near complete reduction of *de novo* SAM production at doses above cellular IC_{50} for SAM (Figures 1C and 1D) with an IC_{50} of 6.2 nM for $^{13}\text{C}_5$, ^{15}N -SAM biosynthesis inhibition (Figure S1B). We performed local pathway tracing with U- $^{13}\text{C}_5$ -methionine to

characterize the impact of AGI-24512 on metabolic pathways downstream of SAM (Figure S1C), revealing reduced metabolite production in both HCT116 *MTAP*^{-/-} and wild-type cells (referred to hereafter as *MTAP*^{-/-} and WT).

PRMT5 is a methyltransferase that is uniquely sensitive to reductions in SAM in *MTAP*-deleted cancer cells due to its biochemical properties such as low K_i for the MTAP substrate MTA combined with relatively low binding affinity for SAM (Marjon et al., 2016). We therefore tested whether pharmacologic inhibition of MAT2A would impair PRMT5 activity in an *MTAP*-null genotype-selective manner. Levels of PRMT5-dependent symmetric dimethyl arginine (SDMA) marks were assessed in *MTAP*^{-/-} and WT cells following AGI-24512 treatment (Figures 1E and 1F). Consistent with prior results, basal SDMA levels were substantially lower in *MTAP*^{-/-} cells. We also observed significant reduction in SDMA levels (Figures 1E and 1G) upon MTAP inhibition (Singh et al., 2004). AGI-24512 treatment led to a further reduction of SDMA marks in *MTAP*^{-/-} but not in WT cells. Additionally, pharmacologic inhibition of MTAP in WT cells synergized with MAT2A inhibition to dramatically reduce SDMA marks. Dose-response studies using a quantitative assay revealed that AGI-24512 inhibits PRMT5-mediated SDMA marks with an IC_{50} of 95 nM in *MTAP*^{-/-} cells, correlating with the 100 nM IC_{50} for cell-growth inhibition observed in these cells (Figure 1F). In contrast, treatment with a SAM-uncompetitive PRMT5 inhibitor, EPZ015666, led to a dose-dependent decrease of SDMA marks irrespective of the *MTAP* status (Figures 1G and 1H). Thus, potent MAT2A inhibitors induce an *MTAP*-null selective effect on PRMT5 cellular activity that to date has not been observed with pharmacologic inhibitors of PRMT5.

AGI-24512 Blocks Proliferation of *MTAP*-Deleted Cancer Cells *In Vitro*

The effect of AGI-24512 on cell growth was monitored in both *MTAP*^{-/-} and WT cells using an ATP-based proliferation readout and time-lapse imaging of cell confluence (Figures 2A and S2A). AGI-24512 reduced growth of *MTAP*^{-/-} cells (IC_{50} after 96 h of treatment was 100 nM), with no significant effect in WT cells. Additionally, pharmacologic MTAP inhibition in WT cells led to accumulation of MTA (Marjon et al., 2016) and sensitized the cells to antiproliferative effects by AGI-24512 (Figures 2A and S2B). Consistent with prior PF-9366 results (Quinlan et al., 2017), we observed upregulation of MAT2A protein upon treatment with AGI-24512 (Figures 1E and 1F). Notably, this pathway feedback mechanism did not prevent the antiproliferative activity of AGI-24512. We hypothesized that the improved potency of AGI-24512 relative to prior MAT2A inhibitors enabled AGI-24512 to maintain antiproliferative effects despite this cellular adaptation and observed that while AGI-24512 cellular potency initially decreased over time, this effect was self-limiting and plateaued within 40 h (Figure S2C). Finally, *CDKN2A* deletion was not responsible for sensitivity to MAT2A inhibition, as MTAP inhibitor (MTAPi) pretreatment was necessary to reduce growth in *CDKN2A* knockout (KO) HAP1 cells (Figures S2D and S2E).

Thus, AGI-24512 selectively reduced growth of *MTAP*^{-/-} cancer cells, confirming our observations using genetic tools targeting MAT2A (Marjon et al., 2016), suggesting that pharmacologic inhibition of MAT2A enzymatic function represents a viable

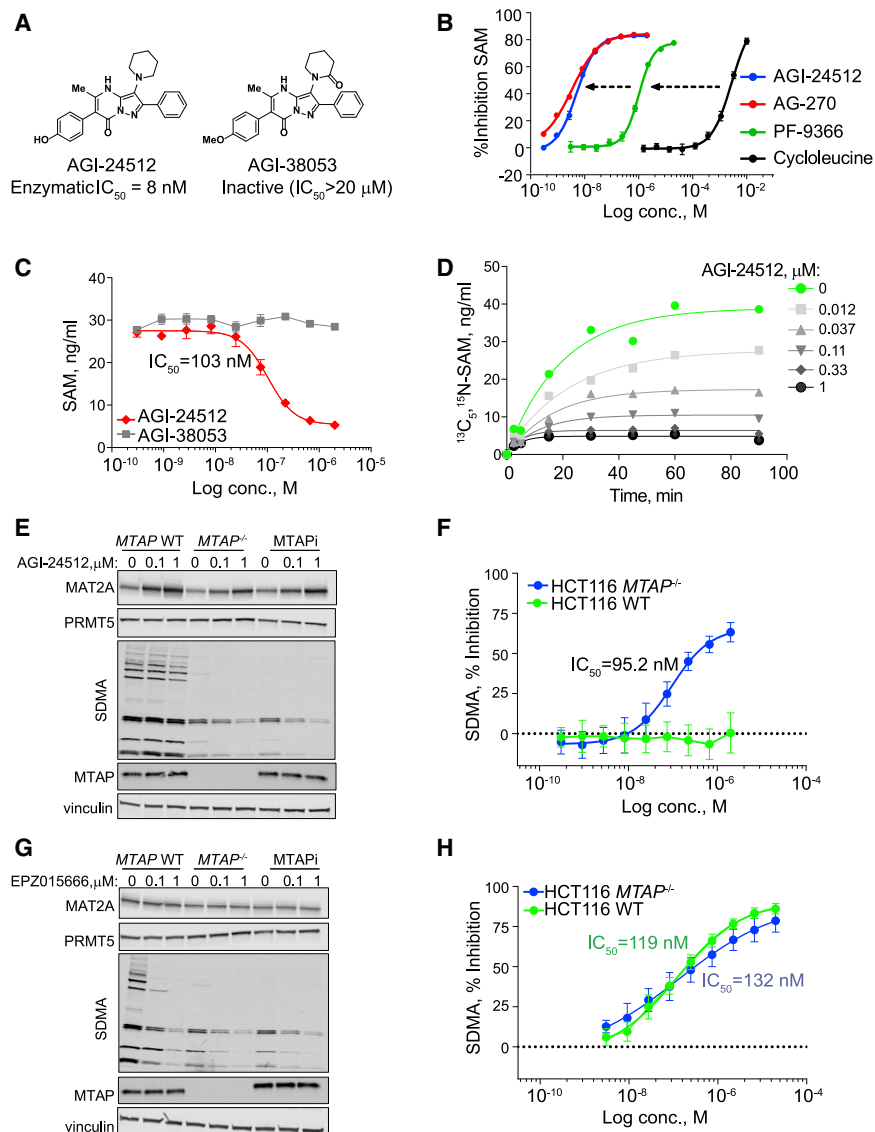


Figure 1. MAT2A Inhibitor AGI-24512 Reduces Cellular S-adenosylmethionine Levels, S-adenosylmethionine De Novo Biosynthesis, and Symmetric Dimethyl Arginine Levels

(A) Structures of AGI-24512 and close analog, AGI-38053, with low-to-no activity in biochemical assay. IC_{50} denotes half maximal inhibitory concentration.

(B) Percent reduction in cellular SAM levels after 4 h of treatment with AGI-24512, AG-270, PF-9366, or cycloleucine (mean \pm SD, n = 3).

(C) Reduction in cellular SAM levels after 72 h of treatment with AGI-24512 or AGI-38053 (mean \pm SD, n = 3). IC_{50} value shown.

(D) Impact of AGI-24512 on the rate of $^{13}C_5, ^{15}N$ -methionine conversion to $^{13}C_5, ^{15}N$ -SAM.

(E and G) Immunoblot analysis of the indicated proteins following treatment with AGI-24512 (E) or EPZ015666 (G) at 1 μ M for 96 h. WT, wild type; MTAPi, methylthioadenosine phosphorylase inhibitor.

(F and H) In-cell western analysis of the reduction in PRMT5-dependent SDMA marks following treatment with AGI-24512 (F) or EPZ015666 (H). Mean \pm SD, with data collected in triplicate from 3–4 independent experiments. IC_{50} value for percent SDMA change versus dimethyl sulfoxide (DMSO) control shown.

See also Figure S1.

therapeutic approach. Next, we explored the antiproliferative effects of AGI-24512 in a panel of 316 cell lines of diverse tumor origins (Figure 2B and Table S1). AGI-24512 inhibited the proliferation of most *MTAP*-deleted lines, with limited effects on most *MTAP* WT lines. Across the panel, *MTAP* deletion predicted sensitivity to AGI-24512, as assessed by growth inhibition (GI_{50} ; $p = 2.6 \times 10^{-13}$) or by growth rate (GR) adjusted metric (GR, 2.2 μ M; $p = 1.4 \times 10^{-15}$) (this metric was chosen arbitrarily; similar results were obtained using additional GR metrics). Furthermore, unbiased bioinformatics analyses revealed that *MTAP* deletion was the genetic feature most predictive of sensitivity to MAT2A inhibition with AGI-24512, and the only other predictive features were deletions of genes adjacent to *MTAP* on chromosome 9p21 (Figures 2C and S2F). Notably, *MTAP*-deleted cell lines were not significantly more sensitive than *MTAP* WT cell lines to the nonspecific cytotoxic agent staurosporine, indicative of the lack of nonspecific vulnerability (Table S1).

While these data suggested that AGI-24512-mediated inhibition of SDMA marks and cancer cell growth were likely on target, we generated drug-resistant cells to further establish the mechanism of AGI-24512 antiproliferative effects. Treatment of *MTAP*-deleted cells with increasing doses of MAT2A inhibitor for 10 weeks led to the emergence of a drug-resistant population. Genome sequencing of this population indicated an A276V point mutation in MAT2A (Figure S2G). Exogenous expression of A276V in treatment-naïve *MTAP*^{-/-} cells indicated that the effects of AGI-24512 are mediated via inhibition of MAT2A (Figures S2H and S2I). AGI-24512 failed to reduce SDMA levels in A276V MAT2A-expressing cells, showing that the effects of AGI-24512 on PRMT5-mediated SDMA marks occur via inhibition of MAT2A (Figure S2J). The drug-resistant A276V mutation is located in the MAT2A allosteric binding pocket (Quinlan et al., 2017 and Agios data on file), suggesting that it could destabilize formation of the drug-enzyme complex.

MAT2A Inhibitors Reduce Growth of *MTAP*-Deleted Cancer Cells *in vivo*

Initial assessment of the pharmacokinetic properties of AGI-24512 indicated poor oral absorption and a short half-life *in vivo*. Structure-guided design and optimization of AGI-24512 generated AG-270, an orally bioavailable and metabolically stable MAT2A inhibitor amenable to *in vivo* work (Figure 3A). AG-270 demonstrated potent reduction in intracellular SAM,

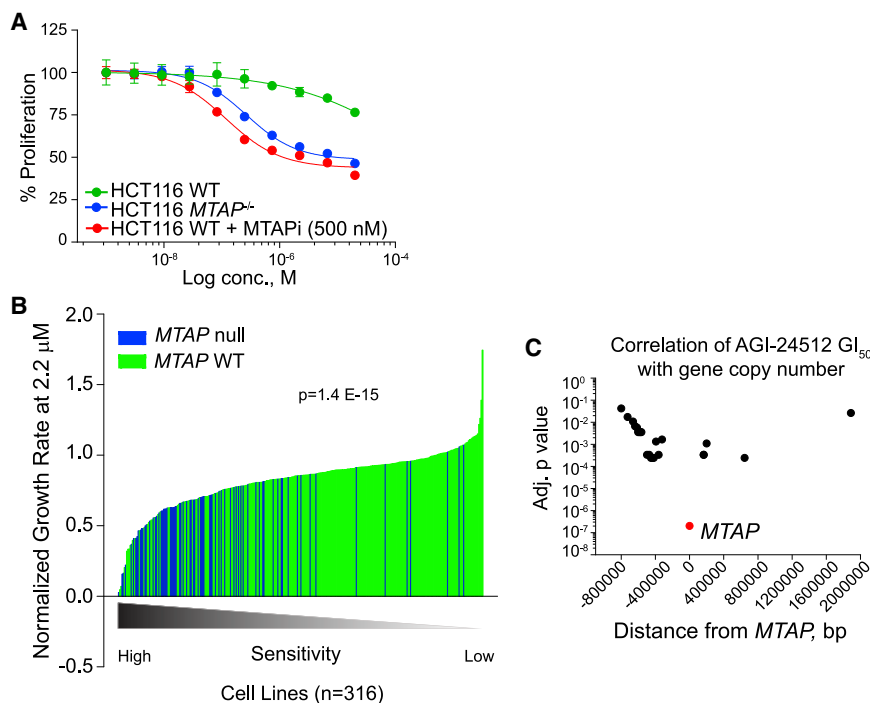


Figure 2. MAT2A Inhibitors Reduce Proliferation of *MTAP*-Deleted and Wild-Type Cell Models *In Vitro*

(A) Percent growth of *MTAP*^{-/-} and WT cells (+/- MTAPi, MTAP inhibitor) upon treatment with AGI-24512 for 96 h (mean \pm SD, n = 3).

(B) Normalized growth rate at 2.2 μ M AGI-24512 in a panel of 316 *MTAP*-deleted or WT cancer cell lines of various tissues of origin.

(C) Correlation of AGI-24512 half-maximal growth inhibitory (GI_{50}) concentrations with various gene copy numbers in the vicinity of *MTAP* locus in the panel from (B). Adjusted (shown as Adj.) p value for each gene is plotted against its genomic distance from the *MTAP* locus. bp, base pairs. See also Figure S2.

cohort allowed us to assess correlations between *MTAP* status and extent of anti-proliferative activity *in vivo*. This analysis highlighted that, similarly to our *in vitro* data, AG-270 reduced growth of most *MTAP*-deleted NSCLC PDX models to a greater extent than *MTAP* WT models (Figure 3C), and this was observed despite the equivalent reduction in intratumoral

MTAP^{-/-}-selective antiproliferative activity, and reduction in SDMA marks with IC_{50} of 50 nM and 35.3 nM, respectively (Figures 1B, 3A, S3A, and S3B). Oral treatment of animals with AG-270 led to sustained high-level exposure in HCT116 xenograft tumors (Figure S3C) with corresponding reductions in levels of SAM (Figure S3D) and was well tolerated. To test whether *MTAP*-null tumors are sensitive to the antiproliferative effects of MAT2A inhibition *in vivo*, we dosed AG-270 orally once daily to mice bearing subcutaneous *MTAP*^{-/-} xenografts (Figures S3E and S3F). Treatment led to a substantial reduction in tumor growth of *MTAP*^{-/-} xenografts (tumor growth inhibition [TGI] = 75%, $p < 0.01$) and was well tolerated, with body weight loss of <20% for all animals. In contrast, no antiproliferative effects were observed in WT tumor-bearing mice. AG-270 led to comparable SAM reductions in both *MTAP*^{-/-} and WT models (Figure S3G), supporting the hypothesis that enhanced reliance on SAM and not differences in SAM production are driving *MTAP*-null selective vulnerability upon MAT2A inhibition. Furthermore, AG-270 treatment reduced SDMA marks in *MTAP*^{-/-} tumors with negligible effects in WT tumors (Figure S3H).

To further explore the effects of AG-270 on tumor growth *in vivo*, we surveyed a panel of patient-derived xenograft (PDX) models from a variety of tumor histological types (Figure 3B and Table S2). PDX models were grown in immunocompromised animals, and established tumors were treated with 200 mg/kg AG-270, which demonstrated maximum target engagement in our HCT116 isogenic pair *in vivo* work. Drug treatment was well tolerated, resulting in reduced tumor growth in a histologically diverse subset of *MTAP*-deleted PDX models, with sustained high drug exposure and reduction in intratumoral SAM levels (Figures S3I and S3J).

Availability of PDX models of both *MTAP* WT and *MTAP*-deleted genotype within the non-small cell lung cancer (NSCLC)

SAM levels (Figure 3D). Critically, analysis of PRMT5 activity in NSCLC models treated with AG-270 highlighted a selective impact on PRMT5-dependent SDMA levels in *MTAP*-deleted models, as measured by our quantitative immunohistochemistry analysis (Figure 3D). This provided proof-of-concept evidence that our observations regarding *MTAP*-null selective effects of MAT2A pharmacologic modulation on PRMT5 cellular activity could be extended to the *in vivo* setting.

While our assessment of AG-270 efficacy across PDX models did not distinguish any particular histological tumor type as more sensitive to MAT2A pharmacologic targeting, we did observe tumor stasis and complete regressions in select tumor models (Figures 3E and 3F).

Finally, assessment of AG-270 specificity in *in vitro* binding assays at 10 μ M using Eurofins' panel of 90 unrelated targets did not reveal any effects exceeding 50% inhibition (Figure S3K).

Pharmacologic Inhibition of MAT2A Leads to *MTAP*^{-/-} Genotype-Selective Cell-Cycle Delays and DNA Damage

We have shown that pharmacologic inhibition of MAT2A enzymatic function represents a viable therapeutic approach yielding antiproliferative activity *in vitro* and *in vivo* in *MTAP*-deleted models. Since combination regimens of cancer therapeutics are often critical for maximal patient benefit (Bayat Mokhtari et al., 2017), we set out to develop rational combination treatment approaches that maximize efficacy of targeting MAT2A in patients with *MTAP*-deleted tumors.

Consistent with antiproliferative responses observed upon AGI-24512 treatment, reduced incorporation of thymidine analog 5-ethynyl-2'-deoxyuridine (EdU) was measured by immunofluorescence analysis in *MTAP*^{-/-} but not WT cells (Figures 4A and 4B). However, no pronounced cell-cycle checkpoint activation was detectable upon MAT2A inhibition in asynchronously proliferating

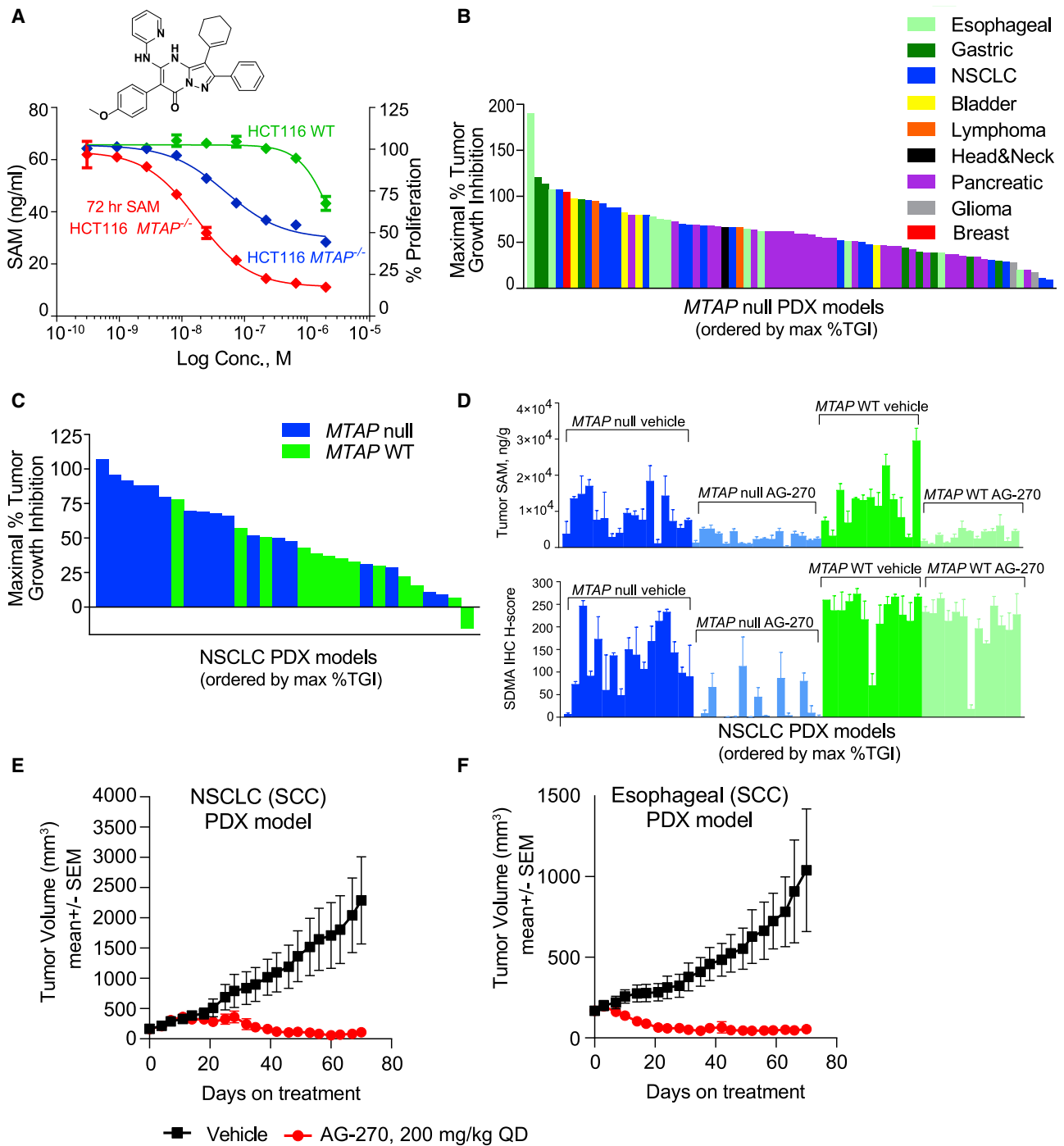


Figure 3. AG-270 Reduces SAM Production *In Vitro* and Reduces Growth of *MTAP*-Deleted and WT Patient-Derived Xenograft Models *In Vivo*
 (A) Reduction in cellular SAM levels after 72 h of treatment (left y axis, red trace) and percent growth after 96 h of treatment (right y axis, *MTAP*^{-/-} with blue trace and WT cells with green trace) with AG-270 (mean ± SD, n = 3).
 (B) Impact of AG-270 on growth of *MTAP*-deleted patient-derived xenograft (PDX) models from a variety of tumor histological types.
 (C) Impact of AG-270 on growth of *MTAP* WT and *MTAP*-deleted genotype within PDX non-small cell lung cancer (NSCLC) cohort.
 (D) Levels of intratumoral SAM and PRMT5-dependent SDMA within NSCLC cohort.
 (E and F) Examples of complete tumor stasis and tumor regression in PDX LU0038 NSCLC (E) and ES0214 esophageal carcinoma (F) models treated with AG-270. TGI, tumor growth inhibition; QD, once daily; SCC, squamous cell carcinoma.
 For all PDX models, n = 3 per group per model; data shown as mean ± SEM. See also Figure S3.

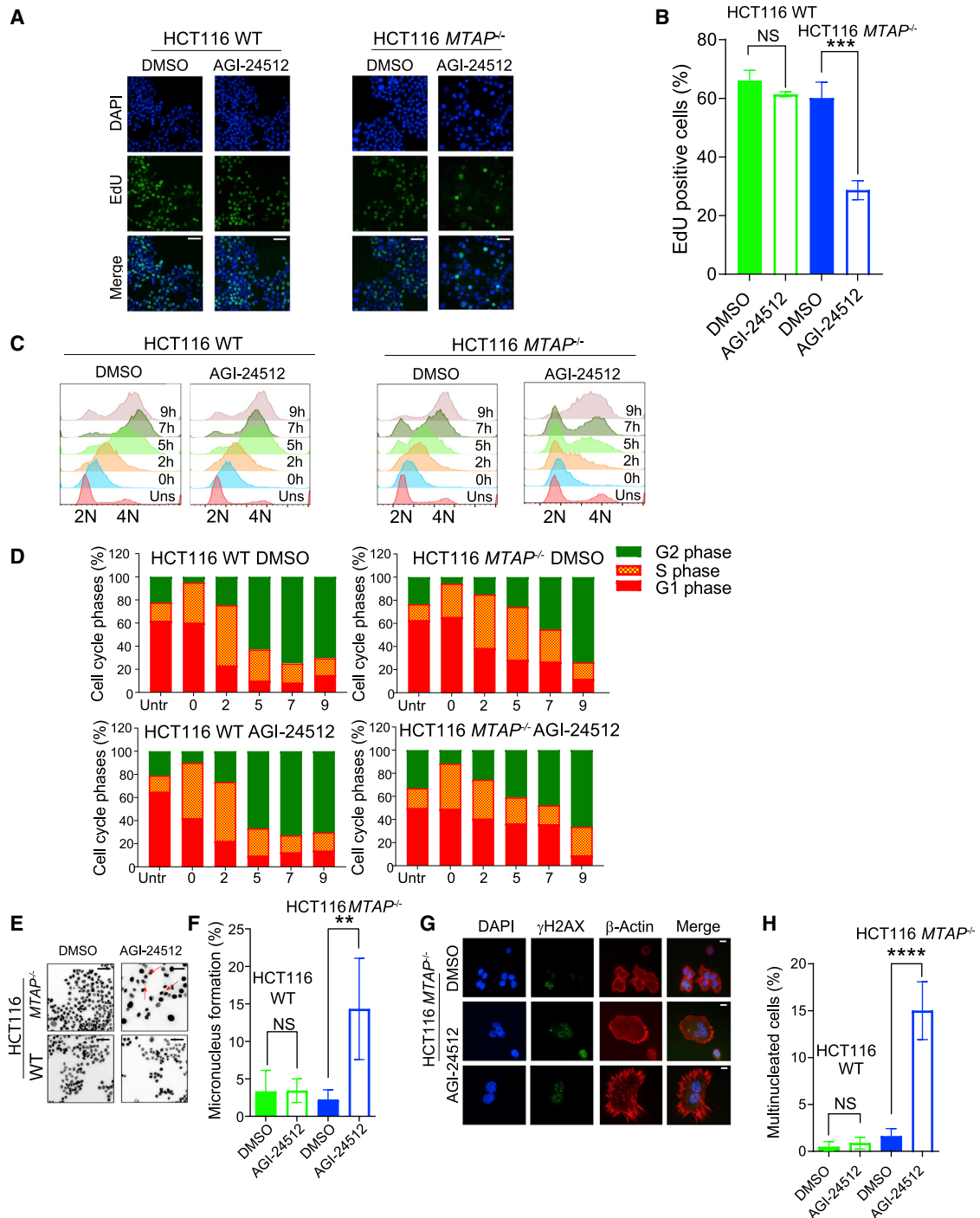


Figure 4. Pharmacologic Inhibition of MAT2A Leads to *MTAP*^{-/-} Genotype-Selective Cell-Cycle Delays and Mitotic Defects

(A and B) Immunofluorescence analysis of 5-ethynyl, 2'-deoxyuridine (EdU) incorporation (A) and quantitative analysis of EdU-positive cells (B) upon treatment with AGI-24512 or DMSO for 6 days (mean \pm SD, n = 3). Scale bar, 50 μ m.

(C and D) Cell-cycle profile histograms (C) and quantitative analysis of cell-cycle distribution (D) after 72 h of pretreatment with 1 μ M AGI-24512 or DMSO followed by double-thymidine block and release for indicated period of time. Uns, unsynchronized, Untr, untreated.

(E and F) 4',6-Diamidino-2-phenylindole (DAPI) staining of micronucleus (E) and quantitative analysis (F) of micronucleus-positive cells upon treatment with AGI-24512 or DMSO (mean \pm SD, n = 5). Scale bar, 50 μ m.

(G and H) DAPI stain with anti- β -actin co-stain demonstrating mitotic defects (G) and quantitative analysis of multinucleated cells (H) upon treatment with AGI-24512 or DMSO (mean \pm SD, n = 10). Scale bar, 10 μ m.

p values were calculated using unpaired Student's t test. **p = 0.01, ***p = 0.001, ****p = 0.0001; NS, not significant. See also Figure S4.

cells. Since cell-cycle alterations induced by AGI-24512 may become more obvious in synchronized cells, we performed double-thymidine block treatment to synchronize cells pretreated with AGI-24512 for 72 h in early S phase (Figure 4C). Upon release from replicative block, we observed significantly attenuated progression of AGI-24512-treated *MTAP*^{-/-} but not of WT cells from G₁ into S and G₂/M phase (Figures 4C and 4D). This attenuated cell-cycle progression correlated with reduced protein levels of several critical regulators of S and G₂/M phase transition, including cyclin B and Aurora kinase B, as well as attenuated appearance of a mitotic marker, phosphorylated histone H3 (Figure S4A). Additionally, levels of CDKN1A/Cip1/p21 (inhibitor of CDK4/6 activity and E2F-driven transcription) were induced upon treatment, consistent with stabilization of p21 upstream regulator p53 (Figure S4A).

These cell-cycle changes were accompanied by chromosomal-level DNA damage, as shown by the formation of micronuclei and appearance of binucleated and multinucleated cells upon treatment with AGI-24512 (Figures 4E–4H). Both micronucleus formation and appearance of multinucleated cells were confined to *MTAP*^{-/-} cells and absent from WT cells.

Reduced proliferation rate, p53 activation, and accumulation of cells with chromosomal abnormalities suggested that AGI-24512 treatment was triggering a DNA damage response (DDR). To assess DDR induction, we analyzed formation of phosphorylated H2AX (γ H2AX) foci as a marker for double-stranded DNA breaks (Figures 5A and 5B). We found a significant increase in γ H2AX-positive cells in *MTAP*^{-/-} cells after treatment with AGI-24512 compared with dimethyl sulfoxide control and WT cells.

We next sought to identify the trigger of DNA damage upon MAT2A inhibition. PRMT5 activity is known to modulate levels of RNA/DNA hybrid structures known as R loops (Zhao et al., 2016), ultimately leading to cellular DNA damage (Paulsen et al., 2009). We used high-throughput immunofluorescence analysis with the R-loop-specific S9.6 antibody to detect whether R-loop formation was induced by MAT2A inhibition with AGI-24512. We detected pronounced and significant increases in R-loop nuclear signal intensity upon AGI-24512 treatment in *MTAP*^{-/-} cells (Figures 5C and 5D). Additional dot blot analysis using the S9.6 antibody demonstrated similar increases in R-loop intensity upon treatment with AGI-24512 in *MTAP*^{-/-} cells (Figures S5A and S5B).

RNAse H is a major regulator of the removal of R loops in eukaryotes (Amon and Koshland, 2016). We generated stable cell lines and observed that overexpression of RNAse H1, but not the catalytically inactive mutant D145N, significantly decreased formation of γ H2AX foci in *MTAP*^{-/-} cells treated with AGI-24512 (Figures 5A and 5B), indicating that R-loop formation is essential for DNA damage induced by MAT2A inhibition.

Importantly, all effects of AGI-24512 including micronucleus formation, γ H2AX foci formation, and R loops were also observed upon direct inhibition of PRMT5 with EPZ015666 but were independent of the *MTAP* genotype (Figures S5C–S5E). Thus, reduction of PRMT5 activity downstream of MAT2A inhibition is sufficient to explain the R-loop formation and DNA damage. Consistent with these findings, overexpression of a PRMT5 mutant (K333R/Y334T) with impaired catalytic activity (Figure S5F) and dominant negative effects in cells (Figure S5G)

sensitized WT cells to MAT2Ai antiproliferative effects (Figure S5H), further supporting the hypothesis that MAT2Ai-induced growth inhibition in *MTAP*-null cells arises due to reduced PRMT5 activity (Kryukov et al., 2016; Marjon et al., 2016; Mavrakis et al., 2016).

Evidence suggests that R-loop formation due to impact on splicing leads to DNA damage upon collision between RNA transcription and DNA replication machineries acting on the same DNA template (Hamperl et al., 2017). Indeed, we observed that MAT2A inhibition resulted in DNA damage in S-phase cells, as supported by co-localization of γ H2AX and EdU signal and collapsed replication fork marker pRPA32 S33 with spliceosome marker SC35 (Figures S5I and S5J). To assess the impact of AGI-24512 on replication fork processivity and replication efficiency, we performed DNA fiber analysis, which showed an increased number of collapsed replication forks in *MTAP*^{-/-} cells after treatment with AGI-24512 (Figures S5K and S5L). Collectively, these data suggest that R loops accumulate upon treatment with AGI-24512, leading to reduced replication rates and DNA damage.

MAT2A Inhibition Leads to Substantial Alterations in RNA Splicing Downstream of PRMT5

Given that MAT2A inhibition leads to reduction of PRMT5 methyltransferase activity in *MTAP*-deleted cancers (Figures 1E and 3D), we assessed the biological consequences of this PRMT5 inhibition.

PRMT5 methylates multiple components of the splicing complex, and PRMT5 inhibition is reported to dysregulate splicing (Bezzi et al., 2013; Braun et al., 2017). We therefore performed RNA sequencing in MAT2A-inhibitor-treated cells to measure gene expression changes and detect splicing changes. We found that AGI-24512 affected multiple alternative splicing events in *MTAP*^{-/-} but not in WT cells (Figures 6A and 6B; Table S3).

While multiple forms of splicing were perturbed upon MAT2A inhibitor treatment, we observed a particularly large increase in transcripts containing a detained intron (DI) (Figures 6A and 6B). This is consistent with recent reports indicating that diverse splicing events including DIs are heavily regulated by PRMT5 activity, and suggest that dysregulated splicing downstream of MAT2A may influence protein expression, since DI-containing transcripts are retained in the nucleus and thus are ineffectively translated (Boutz et al., 2015; Braun et al., 2017). The majority of perturbed DIs were upregulated upon AGI-24512 treatment (Figure 6B), including a number of genes involved in DNA repair. Proteomic analyses revealed that several pathways involved in the DDR were dramatically downregulated by AGI-24512 treatment in *MTAP*^{-/-} cells. Reactome pathway analysis identified the Fanconi anemia (FA) pathway as highly affected, including reductions in the levels of FANCL, FANCA, and FANCD2, but not FANCI (Figure 6C and Table S4).

To determine whether changes to FA pathway proteins were driven by the accumulation of DI transcripts, we performed qRT-PCR, which revealed upregulation of FANCL and FANCA DI-containing transcripts, while total levels of FANCL and FANCA mRNA were reduced (Figure 6D). Upregulation of several other previously reported DI-containing transcripts was confirmed via qRT-PCR using validated

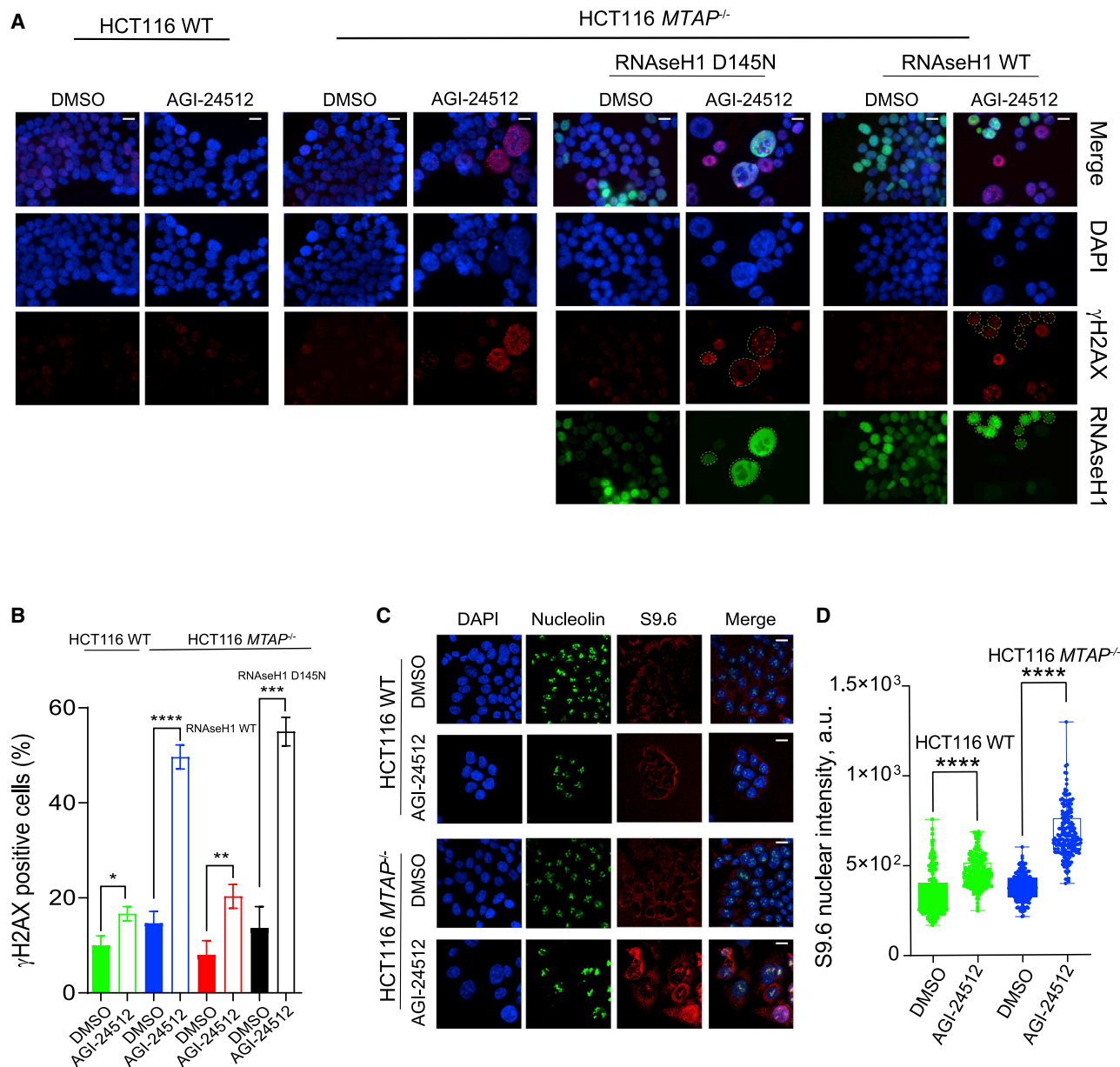


Figure 5. MAT2A Inhibitor AGI-24512 Increases R-Loop Formation and DNA Damage in *MTAP*-Deleted and WT Cell Models

(A and B) Immunostaining (A) and quantitative analysis (B) of γ H2AX-positive cells (%) upon treatment with AGI-24512 or DMSO in WT and *MTAP*^{-/-} cells +/- RNaseH1 WT or RNaseH1 D145N nuclease-dead mutant (mean \pm SD, n = 3).

(C and D) Immunostaining (C) and quantitative analysis (D) of S9.6 nuclear signal intensity upon treatment with AGI-24512 or DMSO (a.u., arbitrary units; 200 individual nuclei are shown; horizontal lines within boxes denote median, edges of boxes the first and fourth quartiles, and whiskers the minimum/maximum values).

p values were calculated using unpaired Student's t test. *p = 0.045, **p = 0.0055, ***p = 0.0002, ****p = 0.0001. Scale bars, 10 μ m. See also Figures S5 and S6.

primers and was observed upon either MAT2A inhibition or direct inhibition of PRMT5 (Figures S6A–S6C). We also confirmed reductions in several FA pathway components by western blot (Figure 6E).

Importantly, inducible RNase H1 overexpression did not rescue splicing defects based on the lack of restoration of FANCA and FANCD2 expression in AGI-24512- or EPZ015666-treated cells (Figure S6D), indicating that this effect of MAT2A in-

hibition is not a consequence of the R-loop-induced DNA damage, but rather is driven by MAT2A/PRMT5-dependent regulation of splicing and DI. Additionally, while AGI-24512-induced DNA damage could be observed as early as 10–24 h after treatment, no significant decline in FA complex components was observed until later (after 48–72 h of treatment, Figures S6E and S8C). These data suggest that AGI-24512 treatment not only triggers DNA damage but also affects the ability of cells to

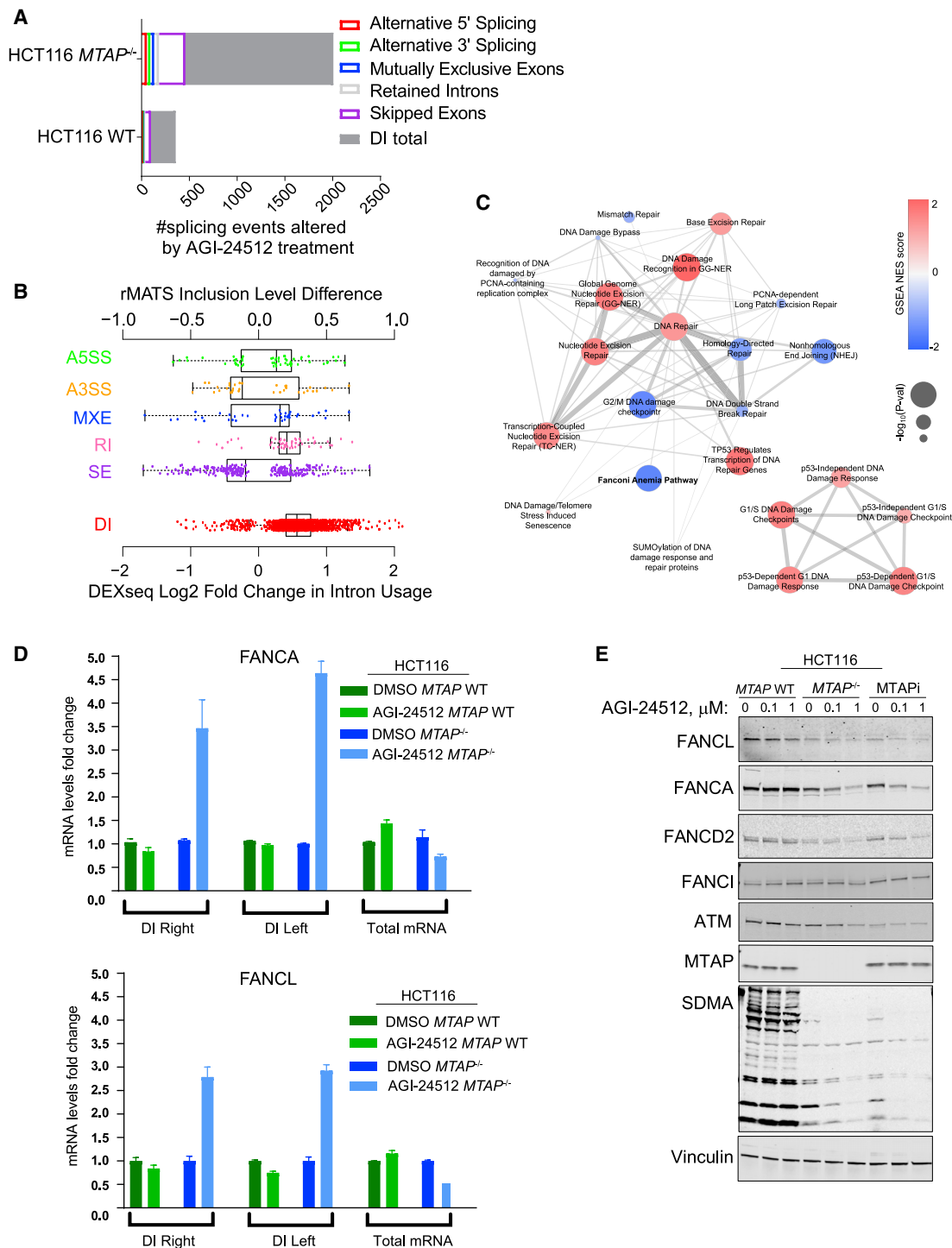


Figure 6. Pharmacologic Inhibition of MAT2A Affects PRMT5 Downstream Splicing Biology

(A and B) rMATS inclusion level differences and DEXseq log₂ fold change in intron usage in *MTAP*^{-/-} (A and B) and WT (A) cells between AGI-24512-treated (1 μM, 6 days) and DMSO control conditions. A5SS, alternative 5' splicing site; A3SS, alternative 3' splicing site; RI, retained introns; SE, skipped exons; MXE, mutually exclusive exons; DI, detained introns. Vertical lines within boxes denote median, edges of boxes the first and fourth quartiles, and whiskers the minimum/maximum values; only statistically significant changes are shown.

(C) Network map of reactome DNA response and repair pathways and impact of AGI-24512 on protein levels. GSEA NES, gene-set enrichment analysis normalized enrichment score; PCNA, proliferating cell nuclear antigen; SUMO, small ubiquitin-like modifier.

(legend continued on next page)

repair it, and both occur through its impact on PRMT5 activity, leading to R-loop accumulation and splicing perturbations.

In Vivo PDX Study Corroborates the Role of DNA Damage Dysregulation as Part of the MAT2A Inhibition-Driven Mechanism

Analysis of sensitivity to MAT2A inhibitor in our large-scale PDX *in vivo* study (Figures 3B–3F) revealed that some models demonstrated better response than others. We next assessed next-generation whole-exome sequencing data of our PDX models to identify potential additional genetic determinants of sensitivity to MAT2A inhibition. This analysis revealed that several of the most sensitive models carried mutations in the *FANCI* gene, and in some cases this was accompanied by the loss of heterozygosity of the second allele (Figures 7A and S7A; Table S5). This finding was intriguing considering our data regarding the impact of *in vitro* tool compound AGI-24152 on FA complex components (Figure 6). As several of the *FANCI* mutations were not previously functionally characterized, we expressed mutant variants in HAP1 *FANCI* KO cells, challenged cells with the DNA cross-linking agent mitomycin C to assess FA complex function, and revealed that the mutations identified in our PDX samples were at least partial loss-of-function (LOF) alleles (Figures S7B and S7C).

In accordance with enhanced *in vivo* responses, we observed that *FANCI* KO HAP1 cells that are deficient in FA pathway activity displayed increased sensitivity to AGI-24512 compared with the parental control when co-treated with MTAPi (Figures 7B and 7C). This was accompanied by the signs of more severe DNA damage and mitotic defects as evidenced by an increased fraction of cells with micronuclei formation, γ H2AX positivity, and multinucleation in HAP1 *FANCI* KO cells treated with AGI-24512 and MTAPi (Figures 7D–7H). Assessment of pH3S10 staining in *FANCI* KO cells clearly demonstrated failed chromosomal segregation and chromosome bridges upon co-treatment with MTAPi and AGI-24512 (Figure 7D). Importantly, while loss of *FANCI* in HAP1 alone was not sufficient to drive R-loop formation, we detected a stronger S9.6 signal in *FANCI* KO MTAP-inhibited cells treated with AGI-24512 (Figures S7D and S7E), consistent with the loss of ability to efficiently resolve these structures (Garcia-Rubio et al., 2015; Okamoto et al., 2019; Schwab et al., 2015). Thus, while the effect of AGI-24512 on R-loop accumulation and induction of DNA damage is FA independent, partial loss of FA complex activity due to perturbed splicing and DI, and especially complete inactivation of FA in LOF genetic backgrounds (*FANCI* KO, *FANCI* LOF mutation), may cooperate with MAT2A inhibition-induced DNA damage, leading to inadequate damage repair and enhanced growth defects.

Finally, we observed that MAT2A inhibition affected additional critical DNA damage regulators with DI, such as ATM kinase, in our models. The impact on ATM was consistent with the sensitizing effects of ATM inhibitor co-treatment on MAT2A inhibition-induced antiproliferative effects (Figures S7F and S7G),

especially in a *FANCI* KO genetic background, in line with reports regarding cooperativity between FA pathway loss and ATM inhibition (Cai et al., 2020). Thus, additional DDR pathway components may play a role in antiproliferative activity upon MAT2A inhibition.

Rational Combination Strategies with AG-270 and Taxanes

The FA complex has mitotic roles (Abdul-Sater et al., 2015; Nalepa et al., 2013), in addition to its role in DNA damage repair during S phase via homologous recombination and R-loop resolution. Deficiency of the most commonly disrupted FA pathway component *FANCA* has been correlated with increased sensitivity to the antimetabolic taxane therapeutic paclitaxel (Abdul-Sater et al., 2015). We hypothesized that reduced levels of FA pathway components triggered by MAT2A inhibition may have a similar sensitizing effect toward taxane-based standard-of-care therapies. Indeed, we observed increased sensitivity of *FANCD2* and *FANCL* KO HAP1 cells to docetaxel and paclitaxel (Figure S8A). We thus tested for AG-270 synergy with taxanes *in vitro* (Chou, 2006) (Figure 8A) and observed a Combination Index of <1, suggestive of a synergistic interaction between AG-270 and docetaxel as well as paclitaxel (Figure 8A) that was selective to *MTAP*^{-/-} cells. Synergy was also observed in the *MTAP*-deleted (*CDKN2A*-deleted) pancreatic cancer cell line KP4 and in the H2122 NSCLC model converted to a functional *MTAP*-inactive state via pretreatment with MTAPi (Figure S8B). As expected, treatment with AG-270 decreased the expression of *FANCA* and *FANCD2* in KP4 cells. Moreover, consistent with reports demonstrating that loss of *FANCA* leads to reduced levels of phospho-H3S10 and multinucleation upon taxol treatment (Abdul-Sater et al., 2015), AG-270 reduced phospho-H3S10, leading to increased numbers of multinucleated cells and increased cleavage of poly(ADP-ribose)polymerase and caspase-3 when combined with either docetaxel or paclitaxel (Figures S8C and S8D).

Encouraged by this *in vitro* synergy between AG-270 and taxanes, we conducted *in vivo* combination treatment studies in NSCLC and esophageal squamous cell carcinoma (SCC) PDX models (Figures 8B and 8C). To facilitate assessment of synergy, we selected two models that were previously identified as only moderately sensitive to MAT2A inhibition alone (Table S2). While modest efficacy was observed upon treatment with either docetaxel (2.5 or 5 mg/kg) or AG-270 (100 mg/kg) alone, complete tumor stasis or regressions were achieved when both agents were combined in both the NSCLC and esophageal models (Figures 8B and 8C). We also observed AG-270 and docetaxel synergy in a KP4-K xenograft model *in vivo*, as well as strong additive effects in another PDX model of pancreatic histology (Figures S8E–S8G). In a separate KP4-K model study with similar *in vivo* observations of synergy between AG-270 and docetaxel, biomarkers of deficient mitosis demonstrated increased frequency of cytomegaly and multinucleated cells in the AG-270/docetaxel

(D) qRT-PCR analysis of the detained intron-containing and total mRNA levels for indicated genes upon treatment with AGI-24512 in HCT116 *MTAP* isogenic pair (mean \pm SD, $n = 3$).

(E) Immunoblot analysis of the indicated proteins in HCT116 *MTAP* isogenic pair and WT cells pretreated with MTAPi upon treatment with AGI-24512 or DMSO for 72 h.

See also Figure S6.

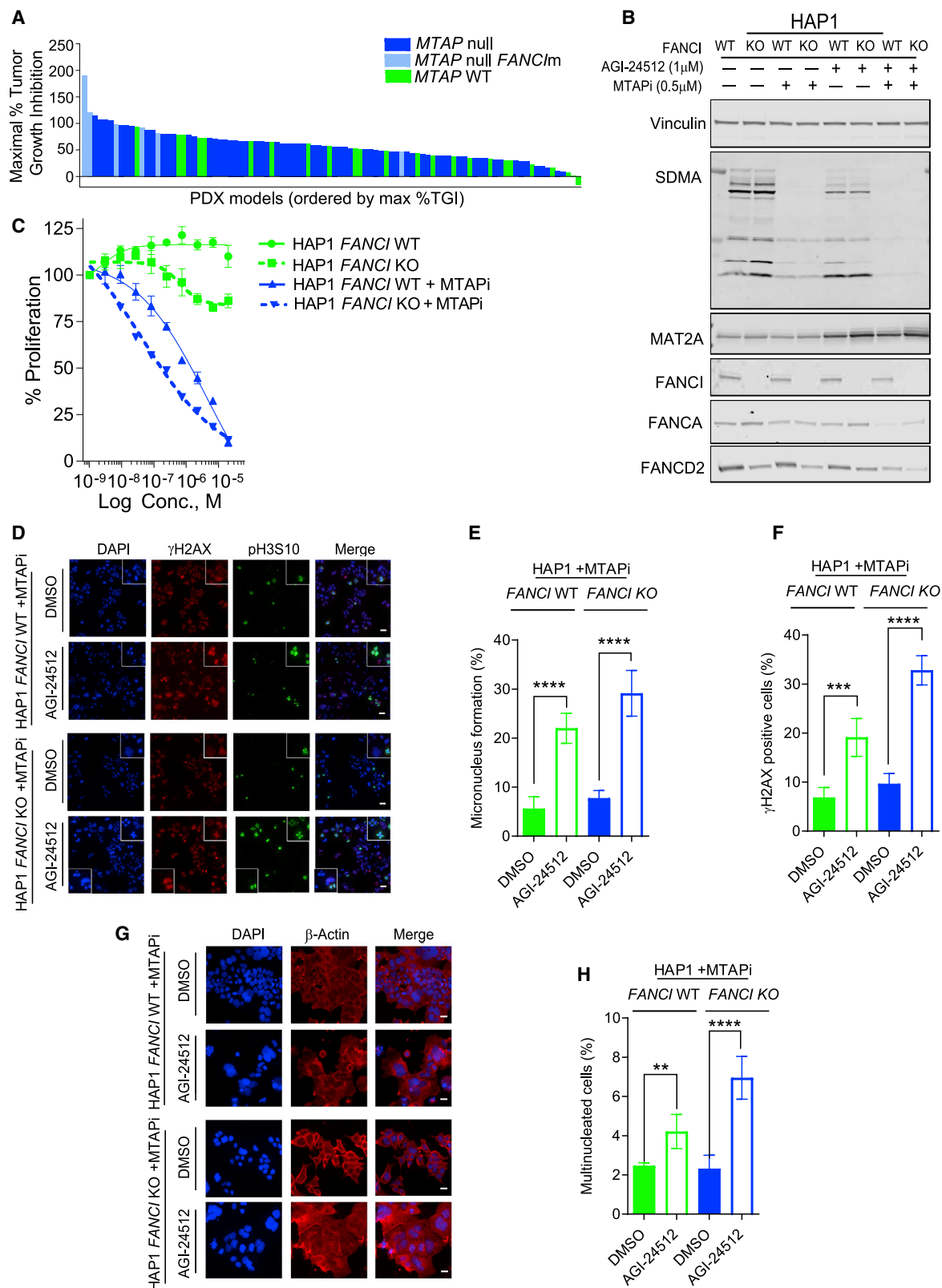


Figure 7. *FANCI* Loss-Of-Function Mutations Increase Sensitivity to MAT2A Inhibition *In Vivo* and *In Vitro*

(A) Impact of *FANCI* mutation status on efficacy of AG-270 treatment in the large-scale PDX *in vivo* study from Figure 3.

(B) Immunoblot analysis of the indicated proteins in HAP1 *FANCI* isogenic pair upon treatment with 1 μ M AGI-24512 with or without 500 nM MTAPi for 72 h.

(C) Percent growth of HAP1 *FANCI* isogenic pair cells (+/- MTAPi) treated with AGI-24512 (mean \pm SD, n = 3).

(legend continued on next page)

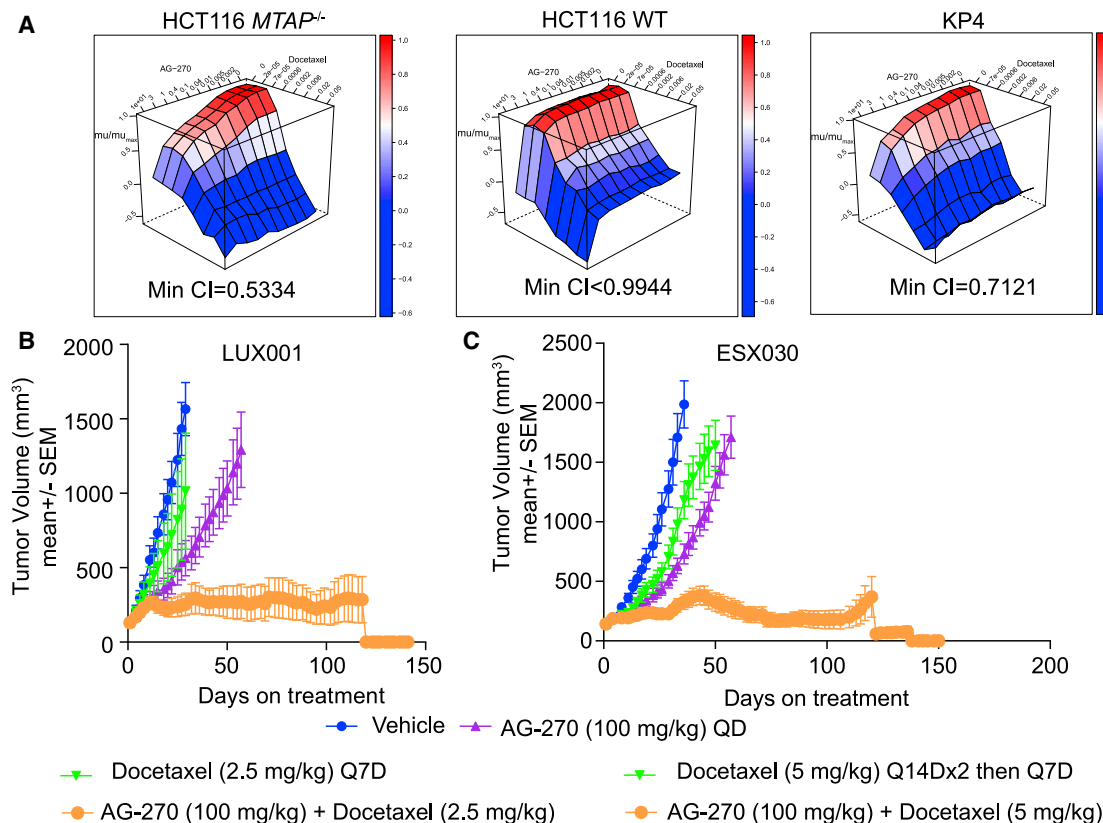


Figure 8. Rational Combination Strategies with AG-270 and Taxanes

(A) Impact of combined treatment with AG-270 and docetaxel on cancer cell growth. Combination Index (CI) < 1 indicates synergy, CI > 1 indicates antagonism, and CI = 1 indicates additive effect of the combination of two drugs. Min CI refers to the lowest CI observed over all the compound concentrations assayed.

(B) Impact of AG-270 and docetaxel alone and in combination on the kinetics of tumor growth in NSCLC-SCC PDX model LUX001 (mean ± SEM, n = 8).

(C) Impact of AG-270 and docetaxel alone and in combination on the kinetics of tumor growth in esophageal-SCC PDX model ESX030 (mean ± SEM, n = 12). QD, dosed daily; Q7D, dosed once a week; Q14Dx2, dosed once every 2 weeks, two cycles of dosing.

See also Figure S8.

combination arm (Figures S8H and S8I). Thus, combination with taxanes, the standard of care for NSCLC, esophageal cancers, and pancreatic cancers, may be an effective clinical strategy for MAT2A inhibitors such as AG-270.

DISCUSSION

Dysregulation of cellular metabolism has been codified as a hallmark of cancer (Hanahan and Weinberg, 2011), leading to many of the earliest anticancer agents, such as antimetabolite therapies, disrupting DNA synthesis (Chabner and Roberts, 2005). While these agents play an important role in cancer therapy, it remains of high interest to identify less toxic options using predictive biomarkers to identify patients likely to benefit from therapy. Targeting oncogenic driver mutations in the metabolic enzymes isocitrate dehydrogenase 1 (IDH1) and IDH2 has proved suc-

cessful (Amatangelo et al., 2017; Kats et al., 2017; Stein et al., 2017; Yen et al., 2017) and has resulted in the recent approval of small-molecule inhibitors of mutant IDH2 and IDH1 for the treatment of patients with refractory/resistant acute myeloid leukemia. However, despite extensive cancer genome sequencing, no additional gain-of-function metabolic oncogenes have been discovered, and designing targeted therapies in cancer metabolism remains a challenge.

Deletion of *CDKN2A/MTAP* is one of the most prevalent oncogenic events across all malignancies, with biallelic deletions occurring in a wide variety of cancers (Beroukhim et al., 2010). While the *CDKN2A* tumor suppressor is the primary oncogenic driver at this locus, *MTAP* resides approximately 100 kb distal to *CDKN2A* and biallelic deletion of *MTAP* occurs in 80%–90% of all *CDKN2A*-deleted tumors (Zhang et al., 1996). Despite this prevalence, very few approaches have been described

(D–F) Immunostaining (D) and quantitative analysis of micronucleus-positive cells (E) and γ H2AX-positive cells (F) in HAP1 *FANCI* isogenic pair upon treatment with MTAPi and AGI-24512 or MTAPi and DMSO (mean ± SD, n = 5). Scale bar, 50 μ m.

(G and H) DAPI stain with anti- β -actin co-stain (G) and quantitative analysis (H) of multinucleated cells in HAP1 *FANCI* isogenic pair treated with MTAPi and AGI-24512 or MTAPi and DMSO (mean ± SD, n = 5). Scale bar, 20 μ m.

p values were calculated using unpaired Student's t test. **p = 0.0059, ***p = 0.0002, ****p = 0.0001. See also Figures S5–S7.

that selectively target *CDKN2A/MTAP*-deleted tumors. Inhibitors of CDK4/CDK6 have been reported to selectively block the growth of *CDKN2A*-deleted cells *in vitro* (Cen et al., 2012; Young et al., 2014), but to date this therapeutic approach has not yielded efficacy in clinical studies. A metabolic strategy to drug *MTAP*-deleted cancers was proposed (Bertino et al., 2011), but this metabolic vulnerability is lost *in vivo*, as tumors uptake circulating adenine, which rescues sensitivity (Rueffli-Brasse et al., 2011).

Previous work investigating *MTAP* loss in cancer cells revealed that MTA accumulation sensitizes cells to short hairpin RNA-mediated depletion of MAT2A as well as the SAM-utilizing enzyme PRMT5. However, existing inhibitors of PRMT5 fail to recapitulate the effects of RNAi-mediated depletion of the target, likely because existing inhibitors have a SAM-uncompetitive mechanism that is not synergistic with MTA and thus fails to leverage MTA elevations that arise in *MTAP*-deleted cancers (Marjon et al., 2016). In contrast, we demonstrate here that reduction of SAM levels via pharmacologic inhibition of MAT2A does act synergistically with MTA elevation and results in further reduction in PRMT5 activity and antiproliferative effects in *MTAP*-deleted cancer cells and tumors. Thus, MAT2A inhibition in cancers with loss of *MTAP/CDKN2A* represents an alternative strategy for precision medicine targeting the human metabolome. The MAT2A/PRMT5 axis essentially allows for the selective inhibition of PRMT5 activity in *MTAP*-deleted cancers by limiting SAM availability, thus MAT2A inhibition might afford a greater therapeutic window than PRMT5 inhibition due to the potential toxicities associated with loss of PRMT5 function in normal physiology (Bezzi et al., 2013; Liu et al., 2015; Tee et al., 2010).

Here, we characterize the orally bioavailable cell- and *in vivo*-active small-molecule inhibitors of MAT2A that entered first-in-human clinical trials, and explore the biological impact of MAT2A inhibition in *MTAP*-deleted cancer models. Specifically, we focus on reduction in PRMT5 activity upon MAT2A inhibition and its impact on downstream cellular processes, such as R-loop formation, DNA damage, and pre-mRNA splicing.

The role of PRMT5 in regulating many key pathways promoting cancer cell proliferation has made it a focus of several recent drug-discovery efforts (Alinari et al., 2015; Chan-Penebre et al., 2015; Kong et al., 2017; Mao et al., 2017; Smil et al., 2015). An emerging theme is the role of PRMT5 in regulating the splicing machinery that profoundly affects critical cell-cycle regulators as well as DDR and repair mechanisms (Bezzi et al., 2013; Braun et al., 2017). Aberrant splicing downstream of PRMT5 inhibition also leads to formation of R loops (Jangi et al., 2017; Li and Manley, 2005; Tanikawa et al., 2016; Zhao et al., 2016), DNA-RNA hybrids that can cause DNA damage (Paulsen et al., 2009; Wan et al., 2015), due to collisions between RNA transcription and DNA replication machineries (Hamperl et al., 2017).

Analysis of pre-mRNA splicing upon MAT2A inhibition showed remarkable similarity to the effects of direct targeting of PRMT5, including severe splicing perturbations in DI. Notably, perturbations were *MTAP*-null selective when targeting MAT2A. These drug-induced splicing defects likely contribute to the antiproliferative effects of MAT2A inhibitors in *MTAP*-null cells. This is supported by our observations of R-loop accumulation and R-loop-dependent DNA damage, which was abrogated by over-expression of the R-loop-resolving enzyme RNase H1. Addition-

ally, FA pathway DNA damage repair proteins function to resolve R loops (Garcia-Rubio et al., 2015; Okamoto et al., 2019), and thus partial loss of FA activity via DI-mediated downregulation upon MAT2A inhibition results in exacerbated DNA damage. Consistently, LOF mutations in *FANCI* that inactivate the FA pathway completely rendered greater sensitivity toward MAT2A inhibition-driven antiproliferative effects. While many other DDR components were affected according to our proteomics analysis and thus potentially play an additional role in antiproliferative effects upon MAT2A inhibition, such as ATM kinase, extensive bioinformatics analysis of both our cell-line panel and PDX *in vivo* studies indicated that mutation of p53 or any other DDR gene fails to significantly affect MAT2A inhibitor sensitivity.

Unresolved DNA replication intermediates may propagate into mitosis especially in an FA-deficient setting, thus contributing to the mitotic defects observed in MAT2A-inhibitor treated cells. Alternatively, mitosis-specific roles of the FA pathway may lead to mitotic defects downstream of MAT2A/PRMT5 inhibition. *FANCD2* and *FANCI* foci can persist into mitosis, localizing to DNA fragile sites that mark the extremities of ultrafine DNA bridges (UFBs) (Chan et al., 2009; Naim and Rosselli, 2009). Increased UFBs and failure to complete cell division was observed in FA pathway-deficient settings (Vinciguerra et al., 2010). Taken together, MAT2A inhibition drives downregulation of PRMT5 activity in cells with dysregulation of splicing and partial FA pathway deficiency. These effects combined may explain DNA damage and mitotic defects downstream of MAT2A inhibition in *MTAP*-deficient background.

Critically, reduced levels of FA pathway components were also reported to sensitize cells to the antimetabolic activity of paclitaxel (Abdul-Sater et al., 2015). We hypothesized that the impact of MAT2A inhibition on FA pathway components and activity may have a similar sensitizing effect toward taxane-based standard-of-care therapies. We have shown that AG-270 synergistically interacts with taxanes in our model systems. Furthermore, MAT2A-induced phenotypes such as multinucleation and inappropriate chromosomal segregation were potentiated by these microtubule stabilizing agents *in vitro* and *in vivo*.

In summary, we describe the mechanism of action of potent cell- and *in vivo*-active inhibitors of MAT2A. Potent MAT2A inhibition is well tolerated and efficacious in *MTAP*-deleted cancers *in vitro* and *in vivo*. Thus, MAT2A inhibitors represent a viable tool to study the biology of MAT2A and SAM in both health and disease, and MAT2A is validated as a therapeutic target for biomarker-directed clinical trials for the substantial patient population with *MTAP*-deleted cancers. Based on these discoveries, the MAT2A inhibitor AG-270 has entered clinical development, and a phase I trial is currently enrolling patients with *MTAP*-deleted solid tumors and lymphomas (Clinical Trial NCT03435250). Furthermore, based on the identified mechanisms driving efficacy upon MAT2A inhibition, we propose that a rational combination approach capitalizing on the synergy between AG-270 and taxanes could be an effective clinical strategy.

STAR★METHODS

Detailed methods are provided in the online version of this paper and include the following:

- **KEY RESOURCES TABLE**
- **RESOURCE AVAILABILITY**
 - Lead Contact
 - Materials Availability
 - Data and Code Availability
- **EXPERIMENTAL MODEL AND SUBJECT DETAILS**
 - Cell Lines
 - Mice
- **METHODS DETAILS**
 - *In Vitro* SAM and *De novo* SAM Biosynthesis Measurement
 - *In Vivo* SAM Measurement by LC-MS/MS
 - Isotopomer Labeling to Assess Metabolic Activity
 - MAT2A and PRMT5 Protein Expression and Purification
 - *In Vitro* Enzymology
 - *In Vitro* SAM and Proliferation Assay
 - *In Vitro* Combination Studies
 - PRMT5 Inhibitor
 - Immunoblotting
 - In-Cell Western Assay
 - Cancer Cell Line Panel Assay
 - Growth Rate and Growth Inhibitory Concentration
 - Correlation of Sensitivity with *MTAP* Genotype
 - Correlation of AGI-24512 GI₅₀ with Copy Number
 - *De novo* SAM Biosynthesis Assay
 - Immunohistochemistry
 - Immunofluorescence
 - Dot Blot Analysis
 - DNA Fiber Analysis
 - Cell Cycle Analysis
 - Splicing Changes from RNAseq Data
 - Cell- and Patient-Derived Xenograft Studies
 - *MTAP* Deletion and Sequencing Analysis in PDX Models
 - Proteomics Analysis
 - Protein Extraction and Digestion
 - Tandem Mass Tag Labeling
 - Basic pH Reverse-Phase HPLC Fractionation
 - Orbitrap Fusion Parameters
 - Mutations and Copy Number Variations in PDX Models
 - Proteomic Data Processing
- **QUANTIFICATION AND STATISTICAL ANALYSIS**

SUPPLEMENTAL INFORMATION

Supplemental Information can be found online at <https://doi.org/10.1016/j.ccell.2020.12.010>.

ACKNOWLEDGMENTS

We thank Sam Reznik and Filippos Kottakis for helpful suggestions and critical review of the manuscript, and Christine Ingleby, PhD, CMPP, Excel Medical Affairs, Horsham, UK (supported by Agios Pharmaceuticals, Inc.) for formatting and editorial assistance. These studies were funded by Agios Pharmaceuticals, Inc.

AUTHOR CONTRIBUTIONS

Conceptualization, K.M. and K.M.M.; Methodology, K.M., P.K., M.L.H., M.F., S.G., J.T., Z.K., M.L., E.A.-F., S.H., and E.S.; Formal Analysis, M.F., J.G.,

and C.-C.C.; Investigation, P.K., M.L.H., S.G., M.L., E.A.-F., V.F., A.B., Y.T., E.M., Y.C., K.S., K.L., R.P., P.Q., M.C., and J.W.; Data Curation, M.F., C.-C.C., and J.G.; Writing – Original Draft, K.M. and K.M.M.; Writing – Review and Editing, K.M., K.M.M., P.K., M.L.H., and M.F.; Visualization, J.G. and C.-C.C.; Supervision, J.M., W.L., R.N., L.D., Z.S., K.M.M., and S.A.B.

DECLARATION OF INTERESTS

The authors are current or past employees and shareholders of Agios Pharmaceuticals, Inc.

PCT/US2020/018036 by Agios Pharmaceuticals, Inc.: Hyer, M.L., Kalev, P., Marjon, K., Marks, K. Combination therapies for use in treating cancer.

Received: February 11, 2020

Revised: October 30, 2020

Accepted: December 10, 2020

Published: January 14, 2021

REFERENCES

- Abdul-Sater, Z., Cerabona, D., Potchanant, E.S., Sun, Z., Enzor, R., He, Y., Robertson, K., Goebel, W.S., and Nalepa, G. (2015). FANCA safeguards interphase and mitosis during hematopoiesis in vivo. *Exp Hematol* **43**, 1031–1046.e12.
- Alinari, L., Mahasenan, K.V., Yan, F., Karkhanis, V., Chung, J.H., Smith, E.M., Quinion, C., Smith, P.L., Kim, L., Patton, J.T., et al. (2015). Selective inhibition of protein arginine methyltransferase 5 blocks initiation and maintenance of B-cell transformation. *Blood* **125**, 2530–2543.
- Amatangelo, M.D., Quek, L., Shih, A., Stein, E.M., Roshal, M., David, M.D., Marteyn, B., Farnoud, N.R., de Botton, S., Bernard, O.A., et al. (2017). Enasidenib induces acute myeloid leukemia cell differentiation to promote clinical response. *Blood* **130**, 732–741.
- Amon, J.D., and Koshland, D. (2016). RNase H enables efficient repair of R-loop induced DNA damage. *eLife* **5**, e20533.
- Anders, S., Reyes, A., and Huber, W. (2012). Detecting differential usage of exons from RNA-seq data. *Genome Res.* **22**, 2008–2017.
- Andrew, S. (2010). FastQC: A Quality Control Tool for High Throughput Sequence Data. <https://www.bioinformatics.babraham.ac.uk/projects/fastqc/>.
- Antonyamy, S., Bonday, Z., Campbell, R.M., Doyle, B., Druzina, Z., Gheyi, T., Han, B., Jungheim, L.N., Qian, Y., Rauch, C., et al. (2012). Crystal structure of the human PRMT5:MEP50 complex. *Proc. Natl. Acad. Sci. U S A* **109**, 17960–17965.
- Barretina, J., Caponigro, G., Stransky, N., Venkatesan, K., Margolin, A.A., Kim, S., Wilson, C.J., Lehar, J., Kryukov, G.V., Sonkin, D., et al. (2012). The Cancer Cell Line Encyclopedia enables predictive modelling of anticancer drug sensitivity. *Nature* **483**, 603–607.
- Bayat Mokhtari, R., Homayouni, T.S., Baluch, N., Morgatskaya, E., Kumar, S., Das, B., and Yeger, H. (2017). Combination therapy in combating cancer. *Oncotarget* **8**, 38022–38043.
- Benjamini, Y.a.Y., D. (2001). The control of the false discovery rate in multiple testing under dependency. *Ann. Stat.* **29**, 1165.
- Beroukhir, R., Mermel, C.H., Porter, D., Wei, G., Raychaudhuri, S., Donovan, J., Barretina, J., Boehm, J.S., Dobson, J., Urashima, M., et al. (2010). The landscape of somatic copy-number alteration across human cancers. *Nature* **463**, 899–905.
- Bertino, J.R., Waud, W.R., Parker, W.B., and Lubin, M. (2011). Targeting tumors that lack methylthioadenosine phosphorylase (MTAP) activity: current strategies. *Cancer Biol. Ther.* **11**, 627–632.
- Bezzi, M., Teo, S.X., Muller, J., Mok, W.C., Sahu, S.K., Vardy, L.A., Bonday, Z.Q., and Guccione, E. (2013). Regulation of constitutive and alternative splicing by PRMT5 reveals a role for Mdm4 pre-mRNA in sensing defects in the spliceosomal machinery. *Genes Dev.* **27**, 1903–1916.

- Boutz, P.L., Bhutkar, A., and Sharp, P.A. (2015). Detained introns are a novel, widespread class of post-transcriptionally spliced introns. *Genes Dev.* **29**, 63–80.
- Braun, C.J., Stanciu, M., Boutz, P.L., Patterson, J.C., Calligaris, D., Higuchi, F., Neupane, R., Fenoglio, S., Cahill, D.P., Wakimoto, H., et al. (2017). Coordinated splicing of regulatory detained introns within oncogenic transcripts creates an exploitable vulnerability in malignant glioma. *Cancer Cell* **32**, 411–426.e11.
- Cai, M.Y., Dunn, C.E., Chen, W., Kochupurakkal, B.S., Nguyen, H., Moreau, L.A., Shapiro, G.I., Parmar, K., Kozono, D., and D’Andrea, A.D. (2020). Cooperation of the ATM and Fanconi anemia/BRCA pathways in double-strand break end resection. *Cell Rep* **30**, 2402–2415.e5.
- Cen, L., Carlson, B.L., Schroeder, M.A., Ostrem, J.L., Kitange, G.J., Mladek, A.C., Fink, S.R., Decker, P.A., Wu, W., Kim, J.S., et al. (2012). p16-Cdk4-Rb axis controls sensitivity to a cyclin-dependent kinase inhibitor PD0332991 in glioblastoma xenograft cells. *Neuro Oncol.* **14**, 870–881.
- Chabner, B.A., and Roberts, T.G., Jr. (2005). Timeline: chemotherapy and the war on cancer. *Nat. Rev. Cancer* **5**, 65–72.
- Chan-Penebre, E., Kuplast, K.G., Majer, C.R., Boriack-Sjodin, P.A., Wigle, T.J., Johnston, L.D., Rioux, N., Munchhof, M.J., Jin, L., Jacques, S.L., et al. (2015). A selective inhibitor of PRMT5 with in vivo and in vitro potency in MCL models. *Nat. Chem. Biol.* **11**, 432–437.
- Chan, K.L., Palmai-Pallag, T., Ying, S., and Hickson, I.D. (2009). Replication stress induces sister-chromatid bridging at fragile site loci in mitosis. *Nat. Cell Biol* **11**, 753–760.
- Chou, T.C. (2006). Theoretical basis, experimental design, and computerized simulation of synergism and antagonism in drug combination studies. *Pharmacol. Rev.* **58**, 621–681.
- Chou, T.C., and Talalay, P. (1984). Quantitative analysis of dose-effect relationships: the combined effects of multiple drugs or enzyme inhibitors. *Adv. Enzyme Regul.* **22**, 27–55.
- Cingolani, P., Platts, A., Wang le, L., Coon, M., Nguyen, T., Wang, L., Land, S.J., Lu, X., and Ruden, D.M. (2012). A program for annotating and predicting the effects of single nucleotide polymorphisms, SnpEff: SNPs in the genome of *Drosophila melanogaster* strain w1118; iso-2; iso-3. *Fly (Austin)* **6**, 80–92.
- Copeland, D. (2006). Evaluation of Enzyme Inhibitors in Drug Discovery: A Guide for Medicinal Chemists and Pharmacologists, 1 edn (Wiley Press).
- Dobin, A., Davis, C.A., Schlesinger, F., Drenkow, J., Zaleski, C., Jha, S., Batut, P., Chaisson, M., and Gingeras, T.R. (2013). STAR: ultrafast universal RNA-seq aligner. *Bioinformatics* **29**, 15–21.
- Edwards, A., and Haas, W. (2016). Multiplexed quantitative proteomics for high-throughput comprehensive proteome comparisons of human cell lines. *Methods Mol. Biol.* **1394**, 1–13.
- Forbes, S.A., Beare, D., Boutselakis, H., Bamford, S., Bindal, N., Tate, J., Cole, C.G., Ward, S., Dawson, E., Ponting, L., et al. (2017). COSMIC: somatic cancer genetics at high-resolution. *Nucleic Acids Res.* **45**, D777–D783.
- Garcia-Rubio, M.L., Perez-Calero, C., Barroso, S.I., Tumini, E., Herrera-Moyano, E., Rosado, I.V., and Aguilera, A. (2015). The Fanconi anemia pathway protects genome integrity from R-loops. *PLoS Genet.* **11**, e1005674.
- Hafner, M., Niepel, M., Chung, M., and Sorger, P.K. (2016). Growth rate inhibition metrics correct for confounders in measuring sensitivity to cancer drugs. *Nat. Methods* **13**, 521–527.
- Hamperl, S., Bocek, M.J., Saldivar, J.C., Swigut, T., and Cimprich, K.A. (2017). Transcription-replication conflict orientation modulates R-loop levels and activates distinct DNA damage responses. *Cell* **170**, 774–786.e19.
- Hanahan, D., and Weinberg, R.A. (2011). Hallmarks of cancer: the next generation. *Cell* **144**, 646–674.
- Hannon, G. (2009). FASTX-Toolkit: FASTQ/A Short Reads Preprocessing Tools. http://hannonlab.cshl.edu/fastx_toolkit/%20.
- Huck, J.J., Zhang, M., Mettetal, J., Chakravarty, A., Venkatakrisnan, K., Zhou, X., Kleinfeld, R., Hyer, M.L., Kannan, K., Shinde, V., et al. (2014). Translational exposure-efficacy modeling to optimize the dose and schedule of taxanes combined with the investigational Aurora A kinase inhibitor MLN8237 (alisertib). *Mol. Cancer Ther.* **13**, 2170–2183.
- Jangi, M., Fleet, C., Cullen, P., Gupta, S.V., Mekhoubad, S., Chiao, E., Allaire, N., Bennett, C.F., Rigo, F., Krainer, A.R., et al. (2017). SMN deficiency in severe models of spinal muscular atrophy causes widespread intron retention and DNA damage. *Proc. Natl. Acad. Sci. U S A* **114**, E2347–E2356.
- Kats, L.M., Vervoort, S.J., Cole, R., Rogers, A.J., Gregory, G.P., Vidacs, E., Li, J., Nagaraja, R., Yen, K.E., and Johnstone, R.W. (2017). A pharmacogenomic approach validates AG-221 as an effective and on-target therapy in IDH2 mutant AML. *Leukemia* **31**, 1466–1470.
- Kong, G.M., Yu, M., Gu, Z., Chen, Z., Xu, R.M., O’Bryant, D., and Wang, Z. (2017). Selective small-chemical inhibitors of protein arginine methyltransferase 5 with anti-lung cancer activity. *PLoS One* **12**, e0181601.
- Kryukov, G.V., Wilson, F.H., Ruth, J.R., Paulk, J., Tsherniak, A., Marlow, S.E., Vazquez, F., Weir, B.A., Fitzgerald, M.E., Tanaka, M., et al. (2016). MTAP deletion confers enhanced dependency on the PRMT5 arginine methyltransferase in cancer cells. *Science* **351**, 1214–1218.
- Li, X., and Manley, J.L. (2005). New talents for an old acquaintance: the SR protein splicing factor ASF/SF2 functions in the maintenance of genome stability. *Cell Cycle* **4**, 1706–1708.
- Liu, F., Cheng, G., Hamard, P.J., Greenblatt, S., Wang, L., Man, N., Perna, F., Xu, H., Tadi, M., Luciani, L., and Nimer, S.D. (2015). Arginine methyltransferase PRMT5 is essential for sustaining normal adult hematopoiesis. *J. Clin. Invest.* **125**, 3532–3544.
- Lombardini, J.B., Coulter, A.W., and Talalay, P. (1970). Analogues of methionine as substrates and inhibitors of the methionine adenosyltransferase reaction. Deductions concerning the conformation of methionine. *Mol. Pharmacol.* **6**, 481–499.
- Lombardini, J.B., and Sufrin, J.R. (1983). Chemotherapeutic potential of methionine analogue inhibitors of tumor-derived methionine adenosyltransferases. *Biochem. Pharmacol.* **32**, 489–495.
- Mao, R., Shao, J., Zhu, K., Zhang, Y., Ding, H., Zhang, C., Shi, Z., Jiang, H., Sun, D., Duan, W., and Luo, C. (2017). Potent, selective, and cell active protein arginine methyltransferase 5 (PRMT5) inhibitor developed by structure-based virtual screening and hit optimization. *J. Med. Chem.* **60**, 6289–6304.
- Marjon, K., Cameron, M.J., Quang, P., Clasquin, M.F., Mandley, E., Kunii, K., McVay, M., Choe, S., Kernytsky, A., Gross, S., et al. (2016). MTAP deletions in cancer create vulnerability to targeting of the MAT2A/PRMT5/RIOK1 Axis. *Cell Rep.* **15**, 574–587.
- Mavrikis, K.J., McDonald, E.R., 3rd, Schlabach, M.R., Billy, E., Hoffman, G.R., deWeck, A., Ruddy, D.A., Venkatesan, K., Yu, J., McAllister, G., et al. (2016). Disordered methionine metabolism in MTAP/CDKN2A-deleted cancers leads to dependence on PRMT5. *Science* **351**, 1208–1213.
- Melamud, E., Vastag, L., and Rabinowitz, J.D. (2020). Metabolomic analysis and visualization engine for LC-MS data. *Anal Chem* **92**, 9818–9826.
- Naim, V., and Rosselli, F. (2009). The FANC pathway and BLM collaborate during mitosis to prevent micro-nucleation and chromosome abnormalities. *Nat. Cell Biol.* **11**, 761–768.
- Nalepa, G., Enzor, R., Sun, Z., Marchal, C., Park, S.J., Yang, Y., Tedeschi, L., Kelich, S., Hanenberg, H., and Clapp, D.W. (2013). Fanconi anemia signaling network regulates the spindle assembly checkpoint. *J. Clin. Invest.* **123**, 3839–3847.
- Nieminuszcz, J., Schwab, R.A., and Niedzwiedz, W. (2016). The DNA fibre technique—tracking helicases at work. *Methods* **108**, 92–98.
- Okamoto, Y., Hejna, J., and Takata, M. (2019). Regulation of R-loops and genome instability in Fanconi anemia. *J. Biochem.* **165**, 465–470.
- Paulsen, R.D., Soni, D.V., Wollman, R., Hahn, A.T., Yee, M.C., Guan, A., Hesley, J.A., Miller, S.C., Cromwell, E.F., Solow-Cordero, D.E., et al. (2009). A genome-wide siRNA screen reveals diverse cellular processes and pathways that mediate genome stability. *Mol. Cell* **35**, 228–239.
- Prabhu, L., Chen, L., Wei, H., Demir, O., Safa, A., Zeng, L., Amaro, R.E., O’Neil, B.H., Zhang, Z.Y., and Lu, T. (2017). Development of an AlphaLISA high throughput technique to screen for small molecule inhibitors targeting protein arginine methyltransferases. *Mol. Biosyst.* **13**, 2509–2520.
- Quinlan, C.L., Kaiser, S.E., Bolanos, B., Nowlin, D., Grantner, R., Karlicek-Bryant, S., Feng, J.L., Jenkinson, S., Freeman-Cook, K., Dann, S.G., et al.

- (2017). Targeting S-adenosylmethionine biosynthesis with a novel allosteric inhibitor of Mat2A. *Nat. Chem. Biol.* *13*, 785–792.
- R Core Team (2017). R: A Language and Environment for Statistical Computing (R Foundation for Statistical Computing).
- Ruefli-Brasse, A., Sakamoto, D., Orf, J., Rong, M., Shi, J., Carlson, T., Quon, K., Kamb, A., and Wickramasinghe, D. (2011). Methylthioadenosine (MTA) rescues methylthioadenosine phosphorylase (MTAP)-deficient tumors from purine synthesis inhibition in vivo via non-autonomous adenine supply. *J. Cancer Ther.* *2*, 523–534.
- Schwab, R.A., Nieminuszczy, J., Shah, F., Langton, J., Lopez Martinez, D., Liang, C.C., Cohn, M.A., Gibbons, R.J., Deans, A.J., and Niedzwiedz, W. (2015). The Fanconi anemia pathway maintains genome stability by coordinating replication and transcription. *Mol. Cell* *60*, 351–361.
- Shcherbo, D., Merzlyak, E.M., Chepurnykh, T.V., Fradkov, A.F., Ermakova, G.V., Solovieva, E.A., Lukyanov, K.A., Bogdanova, E.A., Zaraisky, A.G., Lukyanov, S., and Chudakov, D.M. (2007). Bright far-red fluorescent protein for whole-body imaging. *Nat Methods* *4*, 741–746.
- Shen, S., Park, J.W., Lu, Z.X., Lin, L., Henry, M.D., Wu, Y.N., Zhou, Q., and Xing, Y. (2014). rMATS: robust and flexible detection of differential alternative splicing from replicate RNA-Seq data. *Proc. Natl. Acad. Sci. U S A* *111*, E5593–E5601.
- Shigemizu, D., Momozawa, Y., Abe, T., Morizono, T., Boroevich, K.A., Takata, S., Ashikawa, K., Kubo, M., and Tsunoda, T. (2015). Performance comparison of four commercial human whole-exome capture platforms. *Sci. Rep.* *5*, 12742.
- Singh, V., Shi, W., Evans, G.B., Tyler, P.C., Furneaux, R.H., Almo, S.C., and Schramm, V.L. (2004). Picomolar transition state analogue inhibitors of human 5'-methylthioadenosine phosphorylase and X-ray structure with MT-immucillin-A. *Biochemistry* *43*, 9–18.
- Smil, D., Eram, M.S., Li, F., Kennedy, S., Szewczyk, M.M., Brown, P.J., Barsyte-Lovejoy, D., Arrowsmith, C.H., Vedadi, M., and Schapira, M. (2015). Discovery of a dual PRMT5-PRMT7 inhibitor. *ACS Med. Chem. Lett.* *6*, 408–412.
- Sollier, J., Stork, C.T., Garcia-Rubio, M.L., Paulsen, R.D., Aguilera, A., and Cimprich, K.A. (2014). Transcription-coupled nucleotide excision repair factors promote R-loop-induced genome instability. *Mol. Cell* *56*, 777–785.
- Stein, E.M., DiNardo, C.D., Pollyea, D.A., Fathi, A.T., Roboz, G.J., Altman, J.K., Stone, R.M., DeAngelo, D.J., Levine, R.L., Flinn, I.W., et al. (2017). Enasidenib in mutant IDH2 relapsed or refractory acute myeloid leukemia. *Blood* *130*, 722–731.
- Tanikawa, M., Sanjiv, K., Helleday, T., Herr, P., and Mortusewicz, O. (2016). The spliceosome U2 snRNP factors promote genome stability through distinct mechanisms; transcription of repair factors and R-loop processing. *Oncogenesis* *5*, e280.
- Tee, W.W., Pardo, M., Theunissen, T.W., Yu, L., Choudhary, J.S., Hajkova, P., and Surani, M.A. (2010). Prmt5 is essential for early mouse development and acts in the cytoplasm to maintain ES cell pluripotency. *Genes Dev.* *24*, 2772–2777.
- Vinciguerra, P., Godinho, S.A., Parmar, K., Pellman, D., and D'Andrea, A.D. (2010). Cytokinesis failure occurs in Fanconi anemia pathway-deficient murine and human bone marrow hematopoietic cells. *J. Clin. Invest.* *120*, 3834–3842.
- Wan, Y., Zheng, X., Chen, H., Guo, Y., Jiang, H., He, X., Zhu, X., and Zheng, Y. (2015). Splicing function of mitotic regulators links R-loop-mediated DNA damage to tumor cell killing. *J. Cell Biol.* *209*, 235–246.
- Yen, K., Travins, J., Wang, F., David, M.D., Artin, E., Straley, K., Padyana, A., Gross, S., DeLaBarre, B., Tobin, E., et al. (2017). AG-221, a first-in-class therapy targeting acute myeloid leukemia harboring oncogenic IDH2 mutations. *Cancer Discov.* *7*, 478–493.
- Young, R.J., Waldeck, K., Martin, C., Foo, J.H., Cameron, D.P., Kirby, L., Do, H., Mitchell, C., Cullinane, C., Liu, W., et al. (2014). Loss of CDKN2A expression is a frequent event in primary invasive melanoma and correlates with sensitivity to the CDK4/6 inhibitor PD0332991 in melanoma cell lines. *Pigment Cell Melanoma Res.* *27*, 590–600.
- Zhang, H., Chen, Z.H., and Savarese, T.M. (1996). Codeletion of the genes for p16INK4, methylthioadenosine phosphorylase, interferon-alpha1, interferon-beta1, and other 9p21 markers in human malignant cell lines. *Cancer Genet. Cytogenet.* *86*, 22–28.
- Zhang, J. (2019). CNTools: Convert Segment Data into a Region by Sample Matrix to Allow for Other High Level Computational Analyses. R Package Version 1.46.0. [10.18129/B9.bioc.CNTools](https://doi.org/10.18129/B9.bioc.CNTools).
- Zhao, D.Y., Gish, G., Braunschweig, U., Li, Y., Ni, Z., Schmitges, F.W., Zhong, G., Liu, K., Li, W., Moffat, J., et al. (2016). SMN and symmetric arginine dimethylation of RNA polymerase II C-terminal domain control termination. *Nature* *529*, 48–53.

STAR★METHODS

KEY RESOURCES TABLE

REAGENT or RESOURCE	SOURCE	IDENTIFIER
Antibodies		
Mouse monoclonal anti-Phospho-Histone H2AX	Millipore	Cat# 05-636; RRID: AB_309864
Anti-SC35	Abcam	Cat# 1182; RRID: AB298608
Anti-phospho RPA32 S33	Thermo Fisher Scientific	Cat# A300-246A; RRID: 2180847
Anti-phospho ATM S1981	Cell Signaling Technology	Cat# 4526; RRID: AB2062663
Mouse monoclonal anti-DNA-RNA clone S9.6	Millipore	Cat# MABE1095; RRID: AB2861387
Mouse monoclonal anti-DNA, single stranded	Millipore	Cat# MAB3868; RRID: AB_570342
Rabbit polyclonal anti-Nucleolin	Abcam	Cat# ab22758; RRID: AB_776878
Rabbit anti-SDMA	Cell Signaling Technology	Cat# 13222; RRID: AB_2714013
Rabbit polyclonal anti-PRMT5	Cell Signaling Technology	Cat# 2252; RRID: AB_10694541
Rabbit monoclonal anti-HA-tag	Cell Signaling Technology	Cat# 3724; RRID: AB_1549585
Rabbit monoclonal anti-Phospho-Histone H3 (Ser10)	Cell Signaling Technology	Cat# 53348; RRID: AB_2799431
Rabbit monoclonal anti-p21 Waf/Cip1	Cell Signaling Technology	Cat# 2947; RRID: AB_823586
Rabbit monoclonal anti-Cleaved PARP	Cell Signaling Technology	Cat# 5625; RRID: AB_10699459
Rabbit polyclonal anti-CyclinB1	Cell Signaling Technology	Cat# 4138; RRID: AB_2072132
Rabbit polyclonal anti-AuroraB	Cell Signaling Technology	Cat# 3094; RRID: AB_10695307
Rabbit monoclonal anti-ATM	Cell Signaling Technology	Cat# 2873; RRID: AB_2062659
Rabbit monoclonal anti-Beta-actin	Cell Signaling Technology	Cat# 4970; RRID: AB_2223172
Mouse monoclonal anti-MAT2A	Santa Cruz Biotechnology	Cat# sc-166452; RRID: AB_2266199
Mouse monoclonal anti-MTAP	Santa Cruz Biotechnology	Cat# sc-100782; RRID: AB_2147095
Mouse monoclonal anti-FANCL	Santa Cruz Biotechnology	Cat# sc-137067; RRID: AB_2102346
Rabbit polyclonal anti-H4R3me2s	Epigentek	Cat# A3718
Mouse monoclonal anti-Vinculin	Sigma-Aldrich	Cat# V9131; RRID: AB_477629
Rabbit monoclonal anti-FANCA	Abcam	Cat# AB201457
Rabbit monoclonal anti-FANCD2	Abcam	Cat# ab108928; RRID: AB_10862535
Mouse monoclonal anti-p53	Abcam	Cat# ab1101; RRID: AB_297667
Donkey anti-rabbit IRDye 680RD	LI-COR Biosciences	Cat# 926-68073; RRID: AB_10954442
Donkey anti-mouse IRDye 800CY	LI-COR Biosciences	Cat# 926-32212; RRID: AB_621847
Mouse anti-BRDU	BD Biosciences	Cat# 347580; RRID: AB_10015219
Rat monoclonal anti-BRDU	Abcam	Cat# 6326; RRID: AB_305426
Goat anti-mouse Alexa Fluor 488	Invitrogen	Cat# A32723; RRID: AB_2633275
Goat anti-rabbit Alexa Fluor 555	Invitrogen	Cat# A32732; RRID: AB_2633281
Goat anti-rabbit Alexa Fluor 647	Invitrogen	Cat# A-21245; RRID: AB_2535813
Chemicals, Peptides, and Recombinant Proteins		
AG-270	This Manuscript	N/A
AGI-24512	This Manuscript	N/A
EPZ015666	(Chan-Penebre et al., 2015)	N/A
KU55933	Selleckchem	Cat# S1092
MTAPi	(Singh et al., 2004)	N/A
Docetaxel	Myoderm	Cat# 66758-0050-01
Docetaxel	Selleckchem	Cat# S1148
Paclitaxel	Selleckchem	Cat# S1150

(Continued on next page)

Continued

REAGENT or RESOURCE	SOURCE	IDENTIFIER
DMSO	Sigma-Aldrich	Cat# 276855
CellTag 700	Cell Signaling Technology	Cat# 926-41090
BSA	Cell Signaling Technology	Cat# 9998S
Blocking solution	Roche	Cat# 11096176001
DAPI	Cell Signaling Technology	Cat# 4083
IdU	Sigma-Aldrich	Cat# I7125
CldU	Sigma-Aldrich	Cat# C6891
Vectashield	Vector lab	Cat# H-1000
Acetic acid	Sigma-Aldrich	CAT# 8187552500
Methanol	Sigma-Aldrich	Cat# 34860
Ethanol	Sigma-Aldrich	Cat# 459836
¹³ C ₅ , ¹⁵ N-SAM	Sigma-Aldrich	Cat# 608106
D ₃ -SAM	Sigma-Aldrich	Cat# D4093
Heptafluorobutyric acid	Sigma-Aldrich	Cat# 77249
Acetic acid	Fisher Scientific	Cat# A11350
Formic acid	Fisher Scientific	Cat# A117-50
Ammonium acetate	Fisher Scientific	Cat# A11450
Acetonitrile	Fisher Scientific	Cat# A955-500
Protease/Phosphatase inh cocktail	Cell Signaling Technology	Cat# 5872
PBS	Corning	Cat# 21031CV
Paraformaldehyde solution 4% in PBS	Santa Cruz Biotechnology	Cat# 30525-89-4
HPMCAS-MF	Shin Etsu	N/A
TPGS	Thermo Fisher Scientific	Cat# NC9999736
Odyssey® blocking buffer in TBS	Li-Cor	Cat# 927-50000
Urea	Sigma-Aldrich	Cat# U5378
HEPES pH 8.5	Boston BioProducts	Cat# BBH-85
Trypsin	Promega	Cat# V5280
Propidium Iodide	BD Biosciences	Cat# 556463
Matrigel	Corning	Cat# 356234
TRIzol reagent	ThermoFisher	Cat# 15596026
FuGENE® 6 Transfection Reagent	Promega	Cat# E2691
Hygromycin B	Thermo Fisher Scientific	Cat# 10687010
Polyvinylpyrrolidone (Plasdone PVP K30)	Sigma-Aldrich	Cat# 81420-500G

Critical Commercial Assays

CellTiter-Glo® 2.0 Cell Viability Assay	Promega	Cat# G9241
EnVision Rabbit HRP Detection Kit	Agilent	Cat# K400911-2
Click-iT	Invitrogen	Cat# C10337
BCA assay	Thermo Fisher Scientific	Cat# A53225
PiColorLock Gold kit	Innova Biosciences	N/A
SYBR™ Green PCR Master Mix	Thermo Fisher Scientific	Cat# 4309155
High-Capacity cDNA Reverse Transcription Kit	Thermo Fisher Scientific	Cat# 4368814

Deposited Data

mRNA sequencing data in HCT116 MTAP isogenic pair	Deposited to GEO	GSE161706
Compound structures	PubChem	Compound CIDs 134307780 and 202785

Experimental Models: Cell Lines

Human: HCT116wt and HCT116 MTAP ^{-/-}	Horizon discovery	Cat# HD R02-033
Human: KP4	Riken	Cat# RCB1005
Human: H2122	ATCC	Cat# CRL-5985
Human: Hap1wt and HAP1 FANCI-	Horizon discovery	N/A

(Continued on next page)

Continued		
REAGENT or RESOURCE	SOURCE	IDENTIFIER
Human Hap1 FANCD2-	Horizon discovery	N/A
Human Hap1 FANCL-	Horizon discovery	N/A
Human: Hap1wt and HAP1 CDKN2A-/-	Horizon discovery	Cat# HZGHC003751c011
Human: 293T	ATCC	Cat# CRL-3216
Experimental Models: Organisms/Strains		
Nu/Nu mouse Crl:NU-Foxn1 ^{nu}	Charles River Laboratories	CRL:088, RRID:IMSR_CRL:088
SCID mouse CB17/Icr-Prkdc ^{scid} /IcrIcoCrl	Charles River Laboratories	CRL:236, RRID:IMSR_CRL:236
NOD SCID mouse	Shanghai Lingchang Biotechnology Co., Ltd	N/A
BALB/c nude mouse	GemPharmatech Co., Ltd,	N/A
Nu/Nu mouse	Beijing Vital River Lab Animal Technology Co., Ltd.	N/A
Athymic Nude-Foxn1 ^{nu}	Envigo	N/A
Oligonucleotides		
See Table S6		
Recombinant DNA		
pLVX-IRES-hygro:FANCI-HA S478C	Agios	N/A
pLVX-IRES-hygro:FANCI-HA Q560fs	Agios	N/A
pLVX-IRES-hygro:FANCI-HA D728G	Agios	N/A
pLVX-IRES-hygro:FANCI-HA R884S	Agios	N/A
pLVX-IRES-hygro:FANCI-HA R954T	Agios	N/A
pLVX-IRES-hygro:FANCI-HA Y635C	Agios	N/A
pLVX-IRES-hygro:FANCI-HA N1030Y	Agios	N/A
pLVX-IRES-hygro:FANCI-HA WT	Agios	N/A
pLVX-IRES-hygro:RNaseH-HA WT	Agios	N/A
pLVX-IRES-hygro:RNaseH-HA D145N	Agios	N/A
pLVX-IRES-hygro:Empty Vector	Agios	N/A
psPAX2	Agios	N/A
pCMV-VSVG	Agios	N/A
Software and Algorithms		
Graphpad Prism 8	Graphpad Software	www.graphpad.com/scientific-software/prism/
Image Studio Lite 5	LI-COR	www.licor.com/bio/products/software/image_studio_lite/
FlowJo v10	FlowJo LLC	www.flowjo.com
ImageJ: Image processing and analysis in Java	ImageJ	https://imagej.nih.gov/ij/

RESOURCE AVAILABILITY

Lead Contact

Further information and requests for resources and reagents should be directed to and will be fulfilled by the Lead Contact, Dr. Katya Marjon (katya.marjon@agios.com).

Materials Availability

All unique reagents generated in this study are available from the Lead Contact with a completed Materials Transfer Agreement.

Data and Code Availability

The accession number for the RNA sequencing datasets generated in this study is GEO: GSE161706. The accession numbers for the AGI-24512 and AG-270 structures reported in this paper are PubChem: Compound CID 134307780 and PubChem Compound CID: 202785.

EXPERIMENTAL MODEL AND SUBJECT DETAILS

Cell Lines

HCT116 colon carcinoma parental (WT) cells with *MTAP*^{-/-} isogenic clone and HAP1 fibroblast-like cells (WT) with corresponding *FANCI*, *FANCD2*, *FANCL*, and *CDKN2A* knockout isogenic clone were licensed from Horizon Discovery. All other cell lines were obtained from the American Type Culture Collection (ATCC), RIKEN Bioresource Center cell bank, DSMZ (Deutsche Sammlung von Mikroorganismen und Zellkulturen GmbH), or Japanese Cancer Research Resources Bank (JCRB). All cell lines were cultured in Roswell Park Memorial Institute (RPMI) media supplemented with 10% fetal bovine serum (FBS). Cell line authentication was performed on cells that were used for *in vivo* studies using Short Tandem Repeat (STR) DNA profiling.

Mice

Nu/Nu and female SCID mice (five to six weeks old, Charles River Laboratories) were used for *in vivo* xenograft studies and were cared for in accordance with guidelines approved by an Agios Pharmaceuticals Animal Care and Use Committee (IACUC). Athymic Nude-Foxn1^{nu} mice (Envigo, Indianapolis, IN, USA) were used for *in vivo* PDX efficacy studies conducted at Champions following approved IACUC protocols. Nu/Nu mice (Beijing Vital River Lab Animal Technology Co., Ltd.) were used for *in vivo* PDX efficacy studies conducted at ChemPartner following approved IACUC protocols. BALB/c nude mice (GemPharmatech Co., Ltd, Nanjing, China) or NOD SCID female mice (Shanghai Lingchang Biotechnology Co., Ltd, Shanghai, China) were used for *in vivo* PDX efficacy studies conducted at CrownBio following approved IACUC protocols.

METHODS DETAILS

In Vitro SAM and *De novo* SAM Biosynthesis Measurement

The concentrations of SAM and ¹³C₅, ¹⁵N-SAM in cell samples were determined in HCT116 *MTAP*^{-/-} cells after 4 hr or 72 hr treatment with DMSO control or MAT2A inhibitors as described in figure legends using a non-validated liquid chromatography-tandem mass spectrometry (LC-MS/MS) method as follows. Pelleted cell samples were extracted with 80% cold methanol and 20% water containing 1 M acetic acid and the internal standard D₃-SAM at 100 ng/mL, dried down under vacuum, and reconstituted in 80% acetonitrile, 20% Milli-Q water containing 0.05% formic acid for injection on a LC-MS/MS instrument. SAM was quantified with a surrogate matrix calibration curve of 1 M acetic acid in cold methanol with a dynamic range of 1–500 ng/mL. ¹³C₅, ¹⁵N-SAM was quantified with the surrogate analyte approach using SAM as the surrogate calibration analyte and D₃-SAM as an internal standard; linearity was established from 0.3–500 ng/mL. The peak area ratios of the analyte relative to the internal standard were used for quantitation. Quality control samples were prepared in the same manner as calibration standards, and a quality control sample of HCT116 *MTAP*^{-/-} cells prepared in the same fashion was used to assess longitudinal method performance.

A Waters UPLC Acquity BEH Amide column (2.1x50 mm, 1.7 μm) was used for chromatographic separation at 50°C. A mixture of acetonitrile and water at 5:95 (v/v) with 1% formic acid and 10 mM ammonium acetate (mobile phase A) and a mixture of acetonitrile and water at 95:5 (v/v) with 1% formic acid and 10 mM ammonium acetate (mobile phase B) was employed as the mobile phase at a flow rate of 0.5 mL/min. The linear and stepwise gradient was programmed as follows:

- 0–0.2 minutes: 75% mobile phase B, 25% mobile phase A
- 0.2–0.5 minutes: 75%–35% mobile phase B, 25%–65% mobile phase A
- 0.5–1.0 minutes: 35% mobile phase B, 65% mobile phase A
- 1.0–1.1 minutes: 35%–75% mobile phase B, 65%–25% mobile phase A
- 1.1–2.0 minutes: 75% mobile phase B, 25% mobile phase A

Ionization and detection were performed with an API-6500 Mass Spectrometer (Sciex, Framingham, MA, USA) or Xevo TQ-S Mass Spectrometer (Waters, Milford, MA, USA) in positive ESI mode. SAM and D₃-SAM were detected with multiple-reaction monitoring of a mass transition pair at *m/z* 399.2 → 250.1 and 402.2 → 250.1, respectively. For the SAM *de novo* biosynthesis assay, ¹³C₅, ¹⁵N-SAM was monitored using mass transition pair at *m/z* 405.3 → 250.1.

In Vivo SAM Measurement by LC-MS/MS

The concentration of SAM in plasma and tissue samples was determined using a non-validated LC-MS/MS method as follows. Plasma and tissue samples were stored at -80°C prior to preparation and analysis. Tissue samples were pulverized or cut and weighed in polypropylene tubes. A solution of 1 M acetic acid in cold methanol was added at a 10-fold (w/v) ratio, and the tissue samples were bead homogenized and then spun down with a micro-centrifuge at 4°C, 14,000 RPM for 10 minutes. A calibration curve was prepared containing SAM in a surrogate matrix of 1M acetic acid in methanol with a dynamic range of 10–3,000 ng/mL. Quality control samples were prepared in the same surrogate matrix; additionally, a CD-1 mouse plasma sample (Bioreclamation IVT, Westbury, NY, USA) and pooled HCT116 *MTAP*^{-/-} tumor homogenate prepared in the same way as described above were used to assess longitudinal method performance.

A 15 μL aliquot of calibration standards, quality controls, plasma samples, and the tissue homogenate supernatant was used for each analysis. The samples were extracted with cold methanol containing 1 M acetic acid and the internal standard D₃-SAM at

100 ng/mL, dried down under vacuum, and reconstituted in 80% acetonitrile, 20% Milli-Q water containing 0.05% formic acid for LC-MS/MS detection. SAM was quantified in samples from the calibration curve using the peak area ratio of the analyte relative to the internal standard.

A Waters UPLC Acquity BEH Amide column (2.1x100 mm, 1.7 μ m) was used for chromatographic separation at 50°C. A mixture of acetonitrile and water at 5:95 (v/v) with 1% formic acid and 10 mM ammonium acetate (mobile phase A) and a mixture of acetonitrile and water at 95:5 (v/v) with 1% formic acid and 10 mM ammonium acetate (mobile phase B) was employed as the mobile phase at a flow rate of 0.5 mL/min. The linear and stepwise gradient was programmed as follows:

- 0–0.2 minutes: 75% mobile phase B, 25% mobile phase A
- 0.2–2.5 minutes: 75%–35% mobile phase B, 25%–65% mobile phase A
- 2.5–2.51 minutes: 35%–75% mobile phase B, 65%–25% mobile phase A
- 2.51–3.0 minutes: 75% mobile phase B, 25% mobile phase A

Ionization and detection were performed with an API-6500 Mass Spectrometer (Sciex, Framingham, MA, USA) or Xevo TQ-S Mass Spectrometer (Waters, Milford, MA, USA) in positive ESI mode. SAM and D₃-SAM were detected with multiple-reaction monitoring of a mass transition pair at m/z 399.2 \rightarrow 250.1 and 402.2 \rightarrow 250.1, respectively.

Isotopomer Labeling to Assess Metabolic Activity

To assess metabolic activity through the methionine recycling and salvage pathways, cells were incubated for 72 hrs with 0.2 mM 1:1 [U-13C₅]:[U-12C₅] methionine. After which, media was aspirated and cells were washed with PBS. Metabolism was quenched and metabolites extracted with cold 80/20 (v/v) methanol/water containing 0.1% formic acid. Cells were incubated on dry ice for 15 minutes, centrifuged, and the supernatants were then dried under reduced pressure and stored at –80°C until LC-MS analysis. Prior to injection, dried extracts were reconstituted in LC-MS grade water containing 50 ng/mL acetaminophen as an injection standard. The amount of water was normalized to cell counts.

LC-MS analyses were performed with reversed-phase ion-pairing chromatography coupled by electrospray ionization to a QExactive Orbitrap mass spectrometer (Thermo Fisher Scientific, San Jose, CA). For positive mode ionization, the stationary phase was an Atlantis T3 (3 μ m, 2.1x150 mm) column. LC separation was achieved with a gradient of solvent A (water with 0.1% formic acid and 0.025% heptafluorobutyric acid), and solvent B (acetonitrile with 0.1% formic acid and 0.025% heptafluorobutyric acid). The gradient was 0 min, 0% B; 4 min, 0% B; 6 min, 30% B; 6.1 min, 35% B; 7 min, 100% B; 7.05 min, 100% B; 11 min, 0% B. The flow rate was 200 μ L/min.

For negative mode ionization, the stationary phase was an Acquity HSS T3 (1.8 μ m, 2.1x150 mm) column. LC separation was achieved with a gradient of solvent A (97:3 H₂O/MeOH with 10 mM tributylamine and 15 mM acetic acid, pH 4.95), and solvent B (100% MeOH). The gradient was 0 min, 0% B; 0.5 min, 0% B; 3 min, 20% B; 5.5 min, 20% B; 11 min, 55% B; 13.5 min, 95% B; 16.5 min, 95% B; 17 min, 0% B; 25 min, 0% B. The flow rate was 400 μ L/min.

For both modes, the injection volume was 10 μ L and the QExactive Mass Spectrometer scanned from m/z 70–1000 at a resolving power of 70,000. Data analysis was conducted in MAVEN (Melamud et al., 2010) and Spotfire. Relative quantitation was performed by matching exact mass and retention times to external standards. Untargeted pathway analysis was conducted by classifying metabolites according to the KEGG BRITE database.

MAT2A and PRMT5 Protein Expression and Purification

Human MAT2A protein was expressed by recombinant baculovirus in SF9 infected cells using the Bac to Bac system cloned into the pFASTBAC1 vector (Invitrogen, Carlsbad, CA). Recombinant MAT2A was isolated from the cell lysate of 150 g of infected cells using HP Ni sepharose column chromatography. Recombinant MAT2A homodimer was eluted with 250 and 500 mM imidazole, and fractions containing MAT2A were identified by sodium dodecyl sulfate polyacrylamide gel electrophoresis and pooled.

Recombinant PRMT5 WT and PRMT5 K333R/Y334T were expressed and purified as previously described (Antonyamy et al., 2012).

In Vitro Enzymology

For determination of the inhibitory potency of compounds against the MAT2A homodimer, protein was diluted to 1.25 μ g/mL in assay buffer (50 mM Tris, pH 8.0, 50 mM KCl, 15 mM MgCl₂, 0.3 mM EDTA, 0.005% [w/v] bovine serum albumin [BSA]). Test compound was prepared in 100% dimethyl sulfoxide (DMSO) at 50 \times the desired final concentration. A 1 μ L volume of compound dilution was added to 40 μ L of enzyme dilution and the mixture was allowed to equilibrate for 60 minutes at 25°C. The enzymatic assay was initiated by the addition of 10 μ L of substrate mix (500 μ M ATP, pH 7.0, 400 μ M L-methionine in 1 \times assay buffer), and the mixture was incubated for a further 60 minutes at 25°C. The reaction was halted and the liberated phosphate released by the enzyme in stoichiometric amounts by the production of SAM was measured using the PiColorLock Gold kit (Innova Biosciences, UK). Absolute product amounts were determined by comparison to a standard curve of potassium phosphate buffer, pH 8.0.

Kinetic analysis of PRMT5 WT and double mutant K333R/Y334T in complex with MEP50 was conducted at a constant GL-27 peptide substrate concentration of 50 nM as described (Prabhu et al., 2017). Velocity curves were fit to the standard Michaelis-Menten equation (Copeland, 2006) to yield V_{max} for the WT and mutant.

In Vitro SAM and Proliferation Assay

Two types of assays were conducted in parallel: MAT2A inhibition in cellular environment was monitored by measurement of the abundance of its product, SAM, in HCT116 *MTAP*^{-/-} cells, and cell growth inhibition was monitored in HCT116 WT and *MTAP*^{-/-} cells. HCT116 *MTAP*^{-/-} cells were plated in 96 well tissue culture plates at 20,000 cells per well and allowed to attach overnight at 37°C in 5% CO₂. Compounds were added in a dose response format in 3 rows to generate a 9-point dose response curve in triplicate. Doses were usually started at a 20 μM top concentration with 1:3 serial dilution. Compounds were diluted in DMSO to a final concentration of 0.2% DMSO in media. One column on each plate was designated for the 0.2% DMSO control. Cells were incubated with compound for 72 hrs. After this treatment period, medium was removed and cells were extracted for SAM metabolite measurement by LC-MS/MS.

In parallel, both HCT116 WT and HCT116 *MTAP*^{-/-} cells were plated at 2,000 cells/well and treated as described above for 96 hrs in a cell growth assay. Readout of cell proliferation was obtained by measuring total cellular adenosine triphosphate levels using CellTiter-Glo reagent.

GraphPad Prism was used for plotting the graphs, data analysis, and calculation of the concentration of compound that achieved half maximal inhibition (IC₅₀). SAM level change was plotted as measured SAM concentration in ng/ml against log₁₀ of compound concentration in molar (M) units. Curve fitting was performed using a four-parameter logistic regression.

Cell proliferation readout from the CellTiter-Glo (CTG) assay was plotted as percent inhibition of growth (% Growth) against log₁₀ of compound concentration in molar (M) units. Growth Inhibition (%) = 100 × (CTG readout 96 hr_{dose} - AvgCTG readout 96 hr_{blank}) / (CTG readout 96 hr_{DMSO control} - AvgCTG readout 96 hr_{blank}).

In Vitro Combination Studies

Cells were seeded in 96-well plates at a density of 2,000 cells per well. After treatment with the corresponding compounds, cells were analyzed for cell viability on days zero and six, using CellTiter-Glo luminescent assay (Promega) following the manufacturer's instructions. Luminescence was read on a SpectraMax Paradigm (Molecular Devices). The assessment of drug interactions was performed using the Chou-Talalay model (Chou and Talalay, 1984), which allows estimation of the interactions between two drugs in combination studies. According to this model the interactions are estimated from dose-effect data of single and combined treatments and are represented as a Combination Index (CI) score.

The CI is defined as (D1/EDx1) + (D2/EDx2), where EDx1 (or EDx2) is the dose of single agent drug 1 (or drug 2) which produces a selected effect x (such as 50% growth inhibition), and D1 and D2 are doses of drugs 1 and 2 which also produce the effect x when given in combination. For a given pair of compounds, multiple dose combinations were explored (in a matrix design) to identify the D1/D2 pair that give the lowest CI.

If CI < 1, the two drugs have a synergistic effect, and if CI > 1, the drugs have an antagonistic effect. CI = 1 suggests that the drugs have an additive effect.

PRMT5 Inhibitor

PRMT5 inhibitor EPZ015666 was synthesized following the published synthetic protocol (Chan-Penebre et al., 2015).

Immunoblotting

Cells were resuspended in NP40 lysis buffer, containing protease and phosphatase inhibitor cocktails (Cell Signaling Technology). The cell lysates were incubated on ice for 10 minutes, then sonicated and centrifuged at 4°C. Antibodies used were PRMT5 (2252S), HA-tag (3724S), pH3 S10 (53348S), p21 (2947S), Cleaved PARP (5625S), CyclinB1 (4138S), AuroraB (3094S), ATM (2873S), β-actin (3700S) from Cell Signaling Technology. MAT2A (sc-166452), MTAP (sc-100782), FANCI (sc-137067) from Santa Cruz Biotechnology. SDMA antibody developed against H4R3me2s antigen (A-3718, Epigentek), Vinculin (V9131 Sigma), FANCA (ab201457), FANCD2 (ab108928), p53 (ab1101) from Abcam. Secondary antibodies used were IRDye 680RD Donkey anti-Rabbit (926-68073, LI-COR) and IRDye 800CW Donkey anti-Mouse (926-32212, LI-COR).

In-Cell Western Assay

The HCT116 colon carcinoma parental cell line (WT) and *MTAP*^{-/-} isogenic variant cells were plated in 96 well tissue culture plates at 2,000 per well and allowed to attach overnight at 37°C in 5% CO₂. Compounds were added in a dose-response format in 3 rows to generate a 9-point dose-response curve in triplicate. Doses were usually started at a 2 μM top concentration with 1:3 serial dilution. Compounds were diluted in DMSO to a final concentration of 0.2% DMSO in media. One column on each plate was designated for the 0.2% DMSO control. Cells were incubated with compounds for 96 hrs. After this treatment period, medium was removed and cells stained with antibodies against SDMA protein marks (Cell Signaling Technology #13222), as well as with nonspecific cell stain CellTag 700 (Cell Signaling Technology #926-41090). The change in SDMA level for each compound dose and the DMSO control was calculated by normalizing the SDMA signal in each well to the CellTag 700 signal to adjust for the effect of compound treatment on cell number. The SDMA level change was then plotted as SDMA Inhibition (%) (normalized to each cell line DMSO control sample) against log₁₀ of compound concentration in molar (M) units. Curve fitting was performed using a four-parameter logistic regression. The percentage of SDMA inhibition was calculated as follows: SDMA Inhibition (%) = 100 × (1 - SDMA_{dose} / SDMA_{DMSO control}).

Cancer Cell Line Panel Assay

Cancer cell lines were plated in 96 well tissue culture plates and allowed to attach overnight at 37°C in 5% CO₂. AGI-24512 was added in a dose response format in 2 rows to generate a 10-point dose response curve in duplicate. Dose curves were started at a 20 μM top concentration with 1:3 serial dilution. Compounds were diluted in DMSO to a final concentration of 0.2% DMSO in media. One column on each plate was designated for the 0.2% DMSO control. In each assay run, staurosporine (as specificity control) was added at a 2 μM top concentration with 1:3 serial dilution. Cells were incubated with compounds for 6 days. Total cellular ATP levels were measured using CellTiter-Glo reagent on the day of cell plating (time 0-hr readout). After a 6-day treatment period, readout of cell proliferation was obtained again using CellTiter-Glo reagent. ATP standard curve was generated on both day 0 and day 6.

Growth Rate and Growth Inhibitory Concentration

ATP concentrations for wells treated with AGI-24512, staurosporine, and DMSO were calculated by taking the median luminescence of the corresponding wells, subtracting the median blank well value, and multiplying by the slope of the standard curve. Cell lines for which the DMSO-treated control cells did not double at least once during the 6-day experiment were not analyzed further. Normalized growth rate (GR) values (Hafner et al., 2016) were calculated for various doses of AGI-24512 and staurosporine in each cell line, as follows:

$GR = 2^x - 1$, where $x = \log_2(A_{\text{compound}}/A_0) / \log_2(A_{\text{control}}/A_0)$, in which A_{control} and A_{compound} are the final ATP concentrations for cells treated with DMSO control or compound, respectively, and A_0 is the initial ATP concentration for the same cell line.

Growth inhibitory (GI) values were calculated for each cell line and compound dose as follows:

$GI (\%) = 100 \times [(A_{\text{control}} - A_{\text{compound}}) / (A_{\text{control}} - A_0)]$, where A_{control} and A_{compound} are the final ATP concentrations for cells treated with DMSO control or compound, respectively, and A_0 is the initial ATP concentration for the same cell line.

Values of GI_{50} , the concentration of compound that corresponds to half maximal growth inhibitory concentration, were calculated for each compound and cell line as follows:

If the largest GI at any dose was less than 34%, the GI_{50} was set to the maximum dose (20 μM for AGI-24512, 2 μM for staurosporine). Otherwise, the GI values and compound doses were fitted to a 4-parameter log-logistic curve using the *drc* package of the R statistical language (R Core Team, 2017). In a few cases the curve fitting procedure failed and no GI_{50} value was obtained.

If curve fitting was successful but no GI_{50} value could be extracted, it was set to the maximum dose; in these cases, inspection of the fitted data confirmed that 50% GI was not reached at any dose. If the calculated GI_{50} exceeded the maximum dose, it was set to that value.

Correlation of Sensitivity with *MTAP* Genotype

For cell lines of known *MTAP* genotype, GI_{50} and GR values for the 2 genotypes were compared using a 2-sided Wilcoxon rank sum test, implemented in the stats package of the R statistical language (R Core Team, 2017).

Correlation of AGI-24512 GI_{50} with Copy Number

Copy number data for the relevant cell lines were obtained from 2 databases, the Cancer Cell Line Encyclopedia and the Catalogue of Somatic Mutations in Cancer (Barretina et al., 2012; Forbes et al., 2017). Copy numbers were categorized as homozygous deletion, hemizygous deletion, diploid, low gain, or high amplification using each database. If the copy number data for a gene was not correlated with gene expression data from the same database ($r < 0.3$), those data were not used. Also, if the data from the 2 databases for a particular gene and cell line were contradictory, they were not used.

For correlation testing, genes with alterations from diploid copy number in less than 3 cell lines were not considered. A total of 19,506 genes were tested in 291 cell lines. The copy number for each gene in each cell line was assigned a numerical value from 1 to 7, with a value of 1 for homozygous deletion, 2 for homozygous deletion in 1 database and hemizygous deletion in the other, 3 for hemizygous deletion, 4 for diploid, 5 for low gain, 6 for low gain in 1 database and high amplification in the other, and 7 for high amplification. For each gene, the correlation between AGI-24512 GI_{50} and copy number values across the cell lines was assessed with a 2-sided test using Spearman's rho, implemented in the stats package of the R statistical language (R Core Team, 2017). The resulting p values were adjusted for multiple testing using the method of Benjamini and Yekutieli (Benjamini, 2001).

The start coordinate of each gene was obtained from the GRCh38.p7 human genome assembly. For generation of the plot showing p value for each gene compared to its genomic distance from the *MTAP* locus, distances were measured from the start of the *MTAP* gene to the start of each other gene.

De novo SAM Biosynthesis Assay

HCT116 *MTAP*^{-/-} cells were plated in 96 well tissue culture plates and allowed to attach overnight at 37°C in 5% CO₂. AGI-24512 was added the next day, and cells were incubated with the compound or DMSO for 4 hrs (with medium and compound refreshed after 2 hrs of incubation). AGI-24512 was tested at indicated doses and was diluted in DMSO to a final concentration of 0.2% DMSO in medium. After the 4-hr treatment period, cells were re-fed with medium containing ¹³C₅, ¹⁵N-methionine instead of naturally labeled methionine in the presence of compound or DMSO to label intracellular SAM. At 0, 2.5, 5, 7.5, 10, 15, 20, 30, 45, 60, and 90 minutes after the addition of label, cells were quenched and extracted with organic solvents for LC-MS/MS analysis of ¹³C₅, ¹⁵N-SAM and ¹²C₅, ¹⁴N-SAM levels. GraphPad Prism was used for plotting the graphs, data analysis, and calculation of the concentration of compound that achieved half maximal inhibition (IC_{50}) of *de novo* SAM biosynthesis.

Immunohistochemistry

SDMA immunohistochemistry was performed in accordance with Mosaic Laboratories' standard operating procedures. The SDMA (rabbit MultimAB, Catalog# 13222, Cell Signaling, Danvers, MA) immunohistochemistry (IHC) assay was designed and validated to be a laboratory-developed test. After heat-induced epitope retrieval, the procedure for IHC analysis of SDMA was performed using automated detection with EnVision Rabbit HRP Detection Kit (Agilent, Carpinteria, CA) on the Dako Link 48 autostainer (Agilent). Staining was visualized with DAB chromogen.

Immunofluorescence

Cells were plated on cover slips, fixed with 4% paraformaldehyde for 10 minutes at room temperature and permeabilized with ice-cold methanol for 5 minutes at -20°C . The cells were incubated in blocking buffer 3% bovine serum albumin (BSA) in PBS for 30 minutes at room temperature and then with primary mouse monoclonal anti- γH2AX antibody (S139; Millipore, clone JBW301). For R-loops, immunostaining with an ice-cold methanol fixation method and pretreatment with 0.5% triton X-100 in PBS was used. The slides were blocked with blocking reagent (11096176001 Roche) for 30 minutes and incubated with S9.6 mouse monoclonal (MABE1095 Millipore) and rabbit polyclonal anti-Nucleolin (Abcam ab22758). EdU incorporation analysis was performed using Click-iT Alexa Fluor imaging kit (Invitrogen) according to the manufacturer's protocol. Immunofluorescence analysis was performed using 60X objective with Olympus FV1200 Laser Scanning Confocal microscope. High throughput image acquisition was performed using 20X objective with CellInsight High-Content Screening (HCS) Platform. For R-loops, 200 nuclei were assessed per experimental condition, all points were shown. For γH2AX , multiple fields were assessed per experimental condition in triplicate. Data were represented as mean \pm SD.

Dot Blot Analysis

Dot blot analysis was performed as described (Sollier et al., 2014). Genomic DNA was isolated using the DNeasy Blood and Tissue Kit (Qiagen) following the manufacturer's instructions. 1 μg of DNA was spotted directly on a nitrocellulose membrane and UV cross-linked. For detection of RNA/DNA hybrids, membrane was incubated with mouse S9.6 antibody in BSA/TBST (Tween 0.1%) overnight at 4°C . Single-strand DNA was visualized following 10 min DNA denaturation using 0.5 N, NaOH, 1.5 M NaCl and neutralization for another 10 min in 1 M NaCl, 0.5 M Tris-HCl pH7.0. Detection was performed using mouse anti-single-strand DNA antibody in BSA/TBST (Tween 0.1%) overnight at 4°C . Images were acquired and quantified using Image Studio Lite software (Li-COR Biosciences).

DNA Fiber Analysis

Cells were subsequently labeled with 25 mM IdU and 250 mM CldU for 20 minutes, washed with PBS, and harvested for fiber spread preparation according previously described methodology (Nieminuszczy et al., 2016).

Cell Cycle Analysis

Cells were collected and washed with PBS, fixed with 70% ethanol, treated with 100 $\mu\text{g}/\text{mL}$ RNase A, and stained with 50 $\mu\text{g}/\text{mL}$ propidium iodide. Immunostainings were assessed by FACSCanto (Becton Dickinson).

Splicing Changes from RNAseq Data

5×10^5 cells were plated in 10 cm dishes and treated either with DMSO or AGI-24512 for 6 days in triplicates. RNA was extracted using TRIzol isolation method. Samples were sent to BGI for paired end polyA RNA sequencing, obtaining approximately 100-140 million total 100 base reads per sample. Data quality was assessed using FastQC (Andrew, 2010). The first 5 bases of every read were removed using fastx-trimmer (Hannon, 2009) due to low sequence quality, then reads were aligned to the hg38 human genome build using STAR (Dobin et al., 2013).

Splicing changes on AGI-24512 treatment were first determined with rMats version 3.2.5, using reads on target and junction counts (Shen et al., 2014). Additional changes in detained intron usage were determined as follows. The locations of detained introns reported by Braun and colleagues in the U-87 MG cell line, both with and without treatment with PRMT5 inhibitor, were combined with those reported by Boutz and colleagues in human umbilical vein endothelial, hESC, HeLa, and HepG2 cells (Boutz et al., 2015; Braun et al., 2017). We then applied DEXseq (Anders et al., 2012) to our RNAseq data to determine changes in the usage of these detained intron sequences on AGI-24512 treatment. To validate our approach, we applied it to the RNAseq data of Braun and colleagues for U-87 MG cells treated with the PRMT5 inhibitor EPZ015666. Of 1,315 detained intron segments detected by Braun and colleagues in EPZ015666-treated cells only (and therefore presumably upregulated on treatment), our method identified 976 (74%) as being upregulated on treatment. For both rMATS and DEXseq, statistically significant splicing changes were selected using the criterion FDR < 0.05 and are listed in Table S2.

Cell- and Patient-Derived Xenograft Studies

HCT116 *MTAP* WT and HCT116 *MTAP*^{-/-} xenografts were generated by subcutaneously injecting 10e6 cells, resuspended in 150 μL of 1:1 matrigel and RPMI-1640 media, into the right flank of female Nu/Nu mice (five-to-six weeks old) obtained from Charles River Laboratories, maintained in ventilated caging. For the KP4 *in vivo* study, parental KP4 cells were stably transduced with Katushka tag (Shcherbo et al., 2007) and termed KP4-K. Five to six-week-old female SCID mice were obtained from Charles River Laboratories, and then 5e6 cells were resuspended in 100 μL of 1:1 matrigel and RPMI-1640 medium and injected subcutaneously. Once tumors reached 150–250 mm^3 , mice were randomized into vehicle or drug-treated groups. AG-270 or vehicle (6.7 % w/w HPMCAS-MF,

1% w/w PVP K30, 2% w/w TPGS, 0.1% Simethicone) was administered orally daily (QD). In the KP4-K combination experiment, docetaxel (Myoderm, Cat. No. 66758-0050-01) was dosed intravenously (IV) Q7D for 5 doses. Animals receiving both AG-270 and docetaxel received compounds within a 1 hr interval. Body weights were measured daily and tumor volume measured twice weekly using Vernier calipers, and tumor volume calculated using the formula $0.5 \times W \times W \times L$, with results graphed as mean \pm standard error (SEM). At study end, tumors were harvested and flash frozen for further analysis. Tumor growth inhibition (%TGI) was determined by the formula: $\%TGI = (1 - \{Tt/T0 / Ct/C / 1 - \{C0/Ct\}) \times 100$, where Tt = median tumor volume of treated tumor at time t, T0 = median tumor volume of treated tumor at time 0, Ct = median tumor volume of control tumor at time t, and C0 = median tumor volume of control tumor at time 0.

For single-agent AG-270 PDX efficacy studies, animals were randomized into treatment groups (n=3 animals/cohort) when tumor volumes reached 100-300 mm³ and then treated daily with oral (PO) AG-270 (200 mg/kg) or vehicle (6.7% w/w HPMCAS-MF, 1% w/w PVP K30, 2% w/w TPGS, 0.1% Simethicone). Tumor volumes and body weights were recorded twice per week. Tumor volumes were measured in two dimensions using a caliper, and the volume was expressed in mm³ using the formula: $V = (L \times W \times W)/2$, where V is tumor volume, L is tumor length (the longest tumor dimension) and W is tumor width (perpendicular to L). Tumor growth inhibition rate (TGI%) of each dosing group was calculated according to the following formula: $\%TGI = [1 - (TVi - TV0)/(TVvi - TVv0)] \times 100\%$; TVi is average tumor volume of a dosing group on a specific day; TV0 is average tumor volume of a dosing group on the initial day; TVvi is average tumor volume of the vehicle group on a specific day; TVv0 is average tumor volume of the vehicle group on the initial day. % TGI max was recorded as maximum %TGI observed at any time point over the course of efficacy study. Mice were dosed until the mean tumor volume in the vehicle group reached > 1000 mm³ and at the end of study, plasma and tumor tissues were collected 6 hrs after the last dose. Tumor tissue was cut in half, one half snap frozen and the other half prepared using FFPE. Plasma and tumor tissues were analyzed for PK and PD. AG-270 and taxane combination efficacy studies were performed in the following xenograft models: CTG-1194 (Champions), KP4-K (Agiros), ESX030 (ChemPartner), PA0372 (CrownBio), and LUX001 (ChemPartner). Dosing was initiated when mean group tumor volumes were between 130-224 mm³. Docetaxel was dosed IV and paclitaxel dosed intraperitoneally, and combination treatments (taxane and AG-270) were dosed simultaneously within a 1 hr interval. AG-270 was dosed at 100 mg/kg, dosed PO, QD; docetaxel was dosed at 2.5 mg/kg, IV, once weekly for 18 weeks (Q7Dx18). Each model utilized n=12 animals/arm, except the LUX001 experiment which contained n=8 animals/arm.

In the LUX001 experiment, in the combination group, the last day of drug treatment was day 141. Four animals in this group presented with mostly tumor stasis and were removed from the study on day 120. The 4 remaining animals presented with no palpable tumor by day 109 and remained tumor-free until the end of the study, day 141. In the AG-270 groups, several animals presented with body weight loss (BWL) ~20% and were given AG-270 dosing holidays on days 16-21; in the combination group, 2 animals had ~20% BWL, therefore 1 animal was given AG-270 dosing holidays on days 54-59, 65-73, and 77-83, and the second animal was given a AG-270 dosing holiday on days 38-46 and a docetaxel holiday on day 42. Body weight recovered in both animals.

In the ESX030 experiment, docetaxel was dosed at 5 mg/kg, IV, on days 1, 15, and 29, and then Q7D. On day 120, three animals with tumors > 1000 mm³ were removed from the study. The last day of drug treatment was on day 135 and on day 136; three animals with slow-growing tumors were removed from the study. The six remaining mice presented with no palpable tumor by day 120 and remained tumor-free until the end of the study on day 155. In the combination group, 1 of 12 animals displayed BWL > 20% and received AG-270 dosing holidays on days 55-60; BWL recovered.

Combination synergy analysis compared the area under the (mean) tumor growth curves between single agents and combination treatment. Synergy was determined as follows: synergy score <0 and p-value <0.05; antagonism was determined as follows: synergy score >0 and p-value <0.05; otherwise the effect was considered additive (Huck et al., 2014).

MTAP Deletion and Sequencing Analysis in PDX Models

RNAseq and whole-exome next-generation sequencing data from untreated PDX tumors were obtained from the respective vendors and processed using Array Suite (Omicsoft), removing mouse reads as described for the DNAseq data. To determine *MTAP* deletion in PDX models, we inspected the DNAseq (quality value) and RNAseq reads aligned to the *MTAP* gene using the Array Suite genome browser; this allowed us to identify partial deletions. For a subset of the PDX models, the presence or absence of *MTAP* mRNA expression was determined by quantitative reverse transcriptase PCR of two *MTAP* exons in RNA from tumor samples taken at the end of our efficacy study, and these results were perfectly consistent with the RNAseq data obtained for these models from samples taken before the efficacy study.

We confirmed *FANCI* mutational status via Sanger sequencing in all indicated samples, except for the R954T mutation in model CTG1076, which was not detected in a tumor sample taken at the end of our efficacy study, and the R884S mutation in model LU1513, which was detected in a sample taken earlier than our efficacy study but not in a sample taken at the end of the efficacy study.

Proteomics Analysis

In brief, cell pellets were lysed in 8 M urea and cysteines were reduced and alkylated. Proteins were sequentially digested with LysC (1:50 enzyme:substrate, Wako Chemicals) and trypsin (1:100 enzyme:substrate, Thermo Fisher) and desalted by solid phase extraction. Peptide amounts were normalized and labeled with TMT10plex Isobaric Label Reagents (Thermo Fisher). Pooled peptides were fractionated by basic pH reverse phase into a 96-well plate and fractions were consolidated into 24 samples in a checkerboard manner. Peptides were separated on a 50 μ M C18 EASY-Spray column (Thermo Scientific) using a 70 min, 8–28% acetonitrile gradient and spectra were acquired on an Orbitrap Fusion (Thermo Scientific) using a TMT-MS3 method. All .RAW files were pro-

cessed using Proteome Discoverer 2.1.0.81. Quantitation data from razor peptides were excluded and only unique peptides were used for protein quantitation. Each 10-plex contained the same pooled sample labeled with TMT-131 and all relative abundance data were normalized to this channel so as to compare relative protein abundance across 10-plexes.

Unless otherwise stated, all chemicals were from Sigma Aldrich. All water and solvents were Optima LC/MS grade from Thermo Scientific. Methodology adapted from (Edwards and Haas, 2016).

Protein Extraction and Digestion

Cell pellets were lysed in 8 M urea/50 mM HEPES pH8.5 (Alfa Aesar) and treated with nuclease (Thermo Scientific) for 10 minutes at room temperature with constant shaking in a Thermomixer (Eppendorf). Lysates were reduced with 5 mM DTT for 30 minutes at 37°C and cysteine residues alkylated with 15 mM iodoacetamide for 30 minutes at room temperature in the dark. Excess iodoacetamide was quenched with 10 mM DTT for 15 minutes at room temperature in the dark. Protein was extracted by methanol–chloroform precipitation and 2 x 1 mL methanol washes. Pellets were dried and resuspended in 8 M urea/50 mM HEPES pH 8.5. Protein concentrations were measured by BCA assay (Thermo Scientific) prior to protease digestion. 200 µg aliquots of protein were diluted to 2 M urea and digested with LysC (Wako) in a 1:100 enzyme:protein ratio overnight at 30°C. The next morning trypsin (Promega) was added to a final 1:100 enzyme:protein ratio for 6 h at 37°C. Digests were acidified with 10% trifluoroacetic acid (TFA) to a pH ~2 and subjected to solid-phase extraction (SPE) with HyperSep Retain PEP Cartridges (Thermo Scientific). Peptides were resuspended in 200 mM HEPES pH 8.5/10% acetonitrile (ACN) and concentrations were measured by microBCA assay (Thermo Scientific).

Tandem Mass Tag Labeling

Isobaric labeling of peptides was performed using 10-plex tandem mass tag (TMT) reagents (Thermo Scientific). TMT reagents (0.8 mg) were dissolved in 41 µL of anhydrous ACN and 10 µL was added to 50 µg of peptide. Samples were labeled for 2 hrs at room temperature and quenched by the addition of hydroxylamine to 0.5% v/v for 15 minutes. Samples were pooled, acidified with 10% TFA to a pH ~2 and subjected to SPE. 1.08 mg of peptides from 36 protein digests labeled with TMT-131 was spiked into each 10-plex to normalize across 10-plex experiments. Sample usage and protein digests used in pool are described in Table S3.

Basic pH Reverse-Phase HPLC Fractionation

TMT-labeled peptides were subjected to orthogonal basic-pH reverse phase fractionation. Peptides were solubilized in buffer A 10 mM ammonium bicarbonate pH 8.0/5% ACN and separated on a Biobasic C18 column (5 µm particle size, 4.6 mm ID, and 250 mm length, Thermo Scientific) using an Ultimate 3000 HPLC (Thermo Scientific) and a 44 min linear gradient from 12% to 36% ACN in 10 mM ammonium bicarbonate pH 8 (flow rate of 0.8 mL/min), which separated the peptide mixtures into a total of 96 fractions. The 96 fractions were consolidated into 24 samples in a checkerboard manner, acidified with TFA to pH ~2 and vacuum-dried. Each sample was redissolved in 20 µL 5% formic acid (FA)/5% ACN and 2 µL were analyzed by mass spectrometry.

Orbitrap Fusion Parameters

Spectra were acquired on an Orbitrap Fusion (Thermo Scientific) coupled to an Easy-nLC 1200 ultrahigh pressure liquid chromatography (UHPLC) pump (Thermo Scientific). Peptides were separated on a 50 µm C18 EASYspray column (Thermo Scientific) using a 70 min, 8–28% ACN (constant 0.1% FA) gradient with a 300 nL/min flow rate. MS1 spectra were collected in the Orbitrap at a resolution of 60,000, automated gain control (AGC) target of 5e5, and a max injection time of 100 ms. The 10 most intense ions were selected for MS/MS in a data-dependent manner. Precursors were filtered according to charge state (2–6 z), monoisotopic peak assignment, and previously selected peaks were excluded using a dynamic window of 60 seconds with a mass error +/- 10 ppm. MS2 precursors were isolated with a quadrupole mass filter set to a width of 0.5 m/z and detected in the ion trap operated at Rapid scan rate. MS2 spectra were collected at an AGC of 1e4, max injection time of 150 ms, and CID collision energy of 35%. Synchronous-precursor-selection (SPS) was enabled to include the top 10 MS2 fragment ions for MS3 analysis in the Orbitrap at a resolution of 60,000, automated gain control (AGC) target of 5e5, and a max injection time of 250 ms. 50% HCD collision energy was used to ensure TMT reporter detection.

Mutations and Copy Number Variations in PDX Models

For each PDX model from ChemPartner or Crown Bio, either whole-genome or whole-exome DNAseq data from untreated tumor samples was obtained from the respective vendors and processed using Array Suite (OmicSoft, Cary, NC, USA). To remove sequencing reads originating from mouse tissue, we first aligned the data to the OmicSoft mouse B38 reference genome and retained only the non-aligned reads. The OmicSoft human B37.3 reference genome was used for subsequent alignment.

To determine point mutations and small insertions/deletions, we applied the Array Suite implementation of the Sentieon DNAseq pipeline. Joint calling of samples was used, with whole-genome and whole-exome data treated separately; matched normal samples were not available. For PDX models from Champions, we obtained variant calls generated by that vendor (see <https://database.championsoncology.com/about>). All variant calls were then filtered as follows. Variants were annotated using SnpEff (Cingolani et al., 2012) and variant frequencies observed in the 1000 Genomes, ESP6500 and gnomAD population sequencing databases were added using Array Suite. We filtered out variants that were supported by low numbers of reads (less than 5 variant reads or

less than 10 total reads), variants that had no functional effect, and variants that were likely to be germline rather than somatic based on their frequencies in population databases ($>0.1\%$ in 1000 Genomes or ESP6500 or $>5\%$ in gnomAD).

To confirm mutations in the *FANCI* gene identified from the DNaseq data, we prepared genomic DNA from PDX tumor samples taken at the end of the efficacy study. DNA was isolated using a Qiagen DNA extraction kit and samples were submitted for Sanger sequencing of the relevant regions at NeoGenomics (Fort Myers, FL, USA). Also, for PDX models from Crown Bio, we asked that vendor to similarly sequence tumor samples taken prior to our efficacy study, after the same number of passages as the samples used for DNaseq.

Segmented copy numbers were determined using the pipeline included in Array Suite with small pools of approximately process-matched normal samples: for the whole-exome data HapMap samples NA18943 and NA18948 (Shigemizu et al., 2015) and for the whole-genome data 1000 Genomes samples HG00097, HG00110, HG02508, HG03625, and NA18546. For PDX models from Champions, we obtained segmented copy numbers generated by that vendor (see <https://database.championsoncology.com/about>). For all PDX samples, copy numbers for individual genes were determined using the CNTools package (Zhang, 2019), excluding the X and Y chromosomes. Copy number ratios r were interpreted as follows: $r < 0.125$, homozygous deletion; $0.125 \leq r < 0.75$, hemizygous deletion; $1.625 < r \leq 2.5$, low amplification; $r > 2.5$, high amplification.

Proteomic Data Processing

All .RAW files were processed using Proteome Discoverer 2.1.0.81. MS2 spectral assignment was performed using the SEQUEST algorithm using Uniprot Human reference proteome (UP000005640 downloaded 10/05/2016) and a list of known contaminants (CRAPome.org). Mass tolerances were set to 10 ppm for precursor ions, 0.6 Da for MS2 ions, and 20 ppm for MS3 reporter ions. MS2 false discovery rate (FDR) of less than 1% was calculated using the Percolator algorithm. Reporter ion intensities were adjusted to correct for the isotopic impurities of the different TMT reagents (manufacturer specifications). TMT tags on peptide N termini/lysine residues (+229.162932 Da) and carbamidomethylation of cysteine residues (+57.02146 Da) were set as static modifications and methionine oxidation (+15.99492 Da) was set as a variable modification. Signal-to-noise values for all peptides were summed within each TMT channel and each channel was scaled according to the highest channel sum so that the sum abundance of each channel is equal. Peptides were filtered for a minimum sum signal-to-noise value of 160 across all 10 channels. Quantitation data from razor peptides were excluded and only unique peptides were used for protein quantitation.

QUANTIFICATION AND STATISTICAL ANALYSIS

Details of statistical analyses of the various experiments are described in the relevant methods section. If not specified, graphing and statistical analyses were performed in GraphPad Prism. Details of the data points shown are described in the respective figure legends.